Physica D 464 (2024) 134190

Contents lists available at ScienceDirect

Physica D: Nonlinear Phenomena

journal homepage: www.elsevier.com/locate/physd

An experimental and numerical investigation into the sensitivity of Rayleigh–Bénard convection to heat loss through the sidewalls

Hermes Ferialdi, Marcello Lappa *

Department of Mechanical and Aerospace Engineering, University of Strathclyde, James Weir Building, 75 Montrose Street, Glasgow, G1 1XJ, UK

ARTICLE INFO

Communicated by "Dmitry Pelinovsky"

Keywords:
Buoyancy flow
Water
Heat exchange
Instability and bifurcation in fluid dynamics

ABSTRACT

Thermal buoyancy flows and related heat transfer problems play a crucial role in a variety of fields and industrial applications. The present study is structured around the main objective of systematically investigating the response of fluid convection of the Rayleigh–Bénard type to heat loss taking place through the lateral walls of the considered fluid container. We elucidate, both experimentally and numerically, new aspects which deeply affect the dynamics when the classical assumptions of adiabatic or conducting walls cease to be valid. The emerging spatio-temporal behaviors are examined with respect to several parameters or conditions, including the dimensionality of the system (made accessible by dedicated numerical simulations based on the time-dependent and non-linear governing equations), the average temperature of the liquid, the applied temperature difference, the dependence of fluid properties on temperature and the intensity of heat transfer to the ambient. The results reveal the interesting triadic relationship among the heat exchanged through non-thermally controlled walls, the hierarchy of bifurcations displayed by the flow and the related multiplicity of solutions.

1. Introduction

Flows of gravitational origin in non-isothermal fluids are a classical subject of analysis in nonlinear dynamics and the various forms of buoyancy mechanisms (stemming from the different types of thermal conditions that can be imposed at the physical boundaries of these systems) can be regarded as important archetypes in relation to a variety of phenomena. Areas of applications include (but are not limited to) the science of materials [1-10], biology [11], geophysics [12-14], meteorology [15], oceanography, astrophysics [16], etc. As the analysis of the highly non-linear phenomenology underlying all these problems is, in general, a non-trivial task, over the years, specific configurations have been elaborated with the two-fold intent to work on *easy to handle models* while retaining *enough complexity* to do justice to physical reality. Most conveniently, researchers have introduced simplified geometries in order to focus on well-established influential factors and assess the dynamics displayed by the considered system in response to related changes.

Obviously, regular geometric shapes make mathematical analysis and computational aspects simpler. This is clearly the case of polygonal, parallelepipedic and cylindrical containers. These geometries have traditionally been used to study the onset of convection and ensuing hierarchy of bifurcations (up to the emergence of chaos) in fluids *uniformly heated from below and cooled from above* (i.e. the so-called Rayleigh–Bénard convection). This problem has widely been investigated since the seminal experiments originally conducted by Lord Rayleigh more than one hundred years ago [17]. The main outcome of such concerted efforts has been the determination of a general region of stability in the space of parameters for the *infinite layer*, known as the "Busse balloon" [18-21]. Apart from the infinite layer, the canonical model represented by a simple *differentially heated square or cubic cavity*, i.e. an enclosure delimited by parallel and no-slip walls with the same size, has also become over the years a prototypical benchmark for stability analysis and numerical simulations [22-27].

Cavities of such a kind and, more in general, finite-size systems obviously display an additional degree of freedom with respect to idealized models with infinite horizontal extension, i.e. the *thermal boundary conditions that can be set at the lateral walls* (boundaries parallel to the direction of gravity). This flexibility has indeed led to two main lines of inquiry running in parallel in the literature [28,29]. Put simply, the intention to discern the behavior of the system in response to precise thermal stimuli, which feature a relatively simple mathematical representation, has produced two classical models known as the 'adiabatic' or 'conducting' sidewalls.

* Corresponding author.
E-mail address: marcello.lappa@strath.ac.uk (M. Lappa).

https://doi.org/10.1016/j.physd.2024.134190
Received 6 November 2023; Received in revised form 25 April 2024; Accepted 27 April 2024
Available online 6 May 2024

While the former is representative of a situation with *no heat flux through the wall*, the latter corresponds to a solid boundary featuring a *temperature that varies linearly* from a minimum to a maximum value. Notably, though these conditions might be seen as abstractions, they have actually been used to interpret a vast amount of results, including experiments.

There is no doubt that several useful generalizations can be made using these idealized boundary conditions (BCs). Moreover, the unravelling of the Rayleigh-Bnard (RB) stability problem with simplified BCs can certainly be regarded as a necessary first step in the elucidation of the flow transition process. Nevertheless, it should also be pointed out that with such an approach some important questions remain unanswered. The price for the simplicity is that, in many circumstances of practical interest, identifying a direct connection between the model parameters and the physical behavior of the system of interest is not as straightforward as one would imagine.

This is often the case for processes that are very sensitive to thermal conditions and require great amount of precision in setting or controlling the behavior in proximity to the walls delimiting the fluid. It has been argued that using too simplified boundary conditions in the corresponding simulations may obscure real-life phenomena and limit the translational relevance of theoretical or numerical results to reality.

Obviously, with the BCs described above, excluded are any processes that depend on the details of the effective heat transfer taking place through the walls of the fluid container and ensuing heat exchange with the external environment.

Thus, the primary objective of the present study is to provide a way of understanding more realistic situations, and to suggest methods and diagnostics for a concerted analysis of experiments and related numerical simulations. In other words, *our scope is to quantify how the heat exchange through the walls of the container has an impact on the patterning behavior of RB convection and related transition to chaos and how the related hierarchy of bifurcations differs from that obtained in the framework of classical models with simplified BCs*.

Towards this end, in addition to experiments, we have conducted dedicated two-dimensional (2D) and three-dimensional (3D) numerical simulations in the framework of a finite-difference approach.

2. Experimental apparatus and procedure

The experiments have been executed using dedicated hardware, namely a facility expressly conceived for the study thermal convection in various conditions, hereafter simply referred to as the TCFS (Thermal Convection Fluid Science) Test Rig. This apparatus (shown in Fig. 1) can work in combination with fluid containers (FC) made with an acrylic material (Perspex 'boxes') available with different sizes and aspect ratios. Moreover, the relative orientation of these containers with respect to gravity can be changed in an arbitrary way.

As shown in Fig. 1, the TCFS Test Rig essentially consists of two large sub-assemblies: the Rotating Base Assembly, which is responsible for supporting the apparatus and providing the required angle of inclination, and the Thermal Systems Assembly, used to create the temperature gradient across each of the FCs. Isolated from the main body of the test rig are the Fan Support Assemblies. These are standalone assemblies responsible for ensuring that heat is dissipated from the Cooling System Radiators.

Although the TCFS Test Rig has the capability to study a host of thermal-convection phenomena for different relative inclinations of the imposed temperature difference with respect to the direction of gravity, the apparatus essentially has two "fundamental" or "basic" configurations: a vertical orientation and a horizontal orientation. The set-up of the apparatus may be altered to either one of these configurations depending on whether the researcher wishes to study situations for which the dominant temperature gradient is vertical or horizontal.

As shown in Fig. 2, the FC is "sandwiched" between two opposing Cooling System Containers (CSCs), each of which houses a Peltier

Fig. 1. CAD model of the original design of the TCFS Test Rig.

Module and a liquid-based CPU cooler – each CSC is mounted on two Support Frames, whose position can be varied according to the size of the FC being supported. Good thermal contact is ensured by silicone gel, which is applied liberally to prevent the formation of a layer of insulating air between these components.

If the subject of the research is the study of the instabilities in a fluid bounded between hot and cold horizontal surfaces, these experiments are carried out in the Vertical Configuration (Fig. 2). If the operator wishes to record the fluid from a different perspective, the TCFS Test Rig can be rotated about the FC to allow the Microscope to be sited against another face, again ensuring that the observer has the ability to interrogate the fluid behavior from a number of angles.

With the Vertical Configuration, obviously, only a single CSC 'straddles' the two Support Frames, whilst the opposing CSC is suspended below it by connecting rods. Good thermal contact is ensured by tightening the nuts on the four connecting rods, thus pulling the 'suspended' CSC towards the upper CSC and 'squeezing' the FC between the Peltier Modules.

To improve stability, the FC is supported by two pneumatic suction pads with a 12 V vacuum pump being used to generate a vacuum of approximately 5.4×10^4 Pa. In particular, the suction pads, which can be adjusted according to the dimensions of the FC, can be installed on any two of the four remaining faces of the FC (two of the faces being obviously occupied by the CSCs). Moreover, in order to leave the view of the Microscope and the Light Source unobstructed, the pneumatic suction pads are designed to protrude through a slot cut out of each Support Frame.

The TCFS Test Rig has been designed to support the use of three cubic and cuboidal FCs with the following inner dimensions: 40 x 40 x 40 mm^3 (used to conduct the experiments presented in this work), 60 x 60 x 60 mm^3 or 40 x 40 x 90 mm^3. The temperature gradient required for each experiment is produced by up to two opposing Peltier Modules (40 x 40 x 4 mm^3, 12 V, 6A); each is controlled by a Omega CN32PT-440-DC PID Temperature Controller (accurate to +/- 0.2 °C) which uses a 5 kΩ thermistor (accurate to +/- 0.1 °C) mounted against the face of the FC to determine the temperature, thus resulting in an overall temperature accuracy of +/−0.3 °C on the outer surface of the FC. Although the Temperature Controller does come with an inbuilt auto-tuning function,

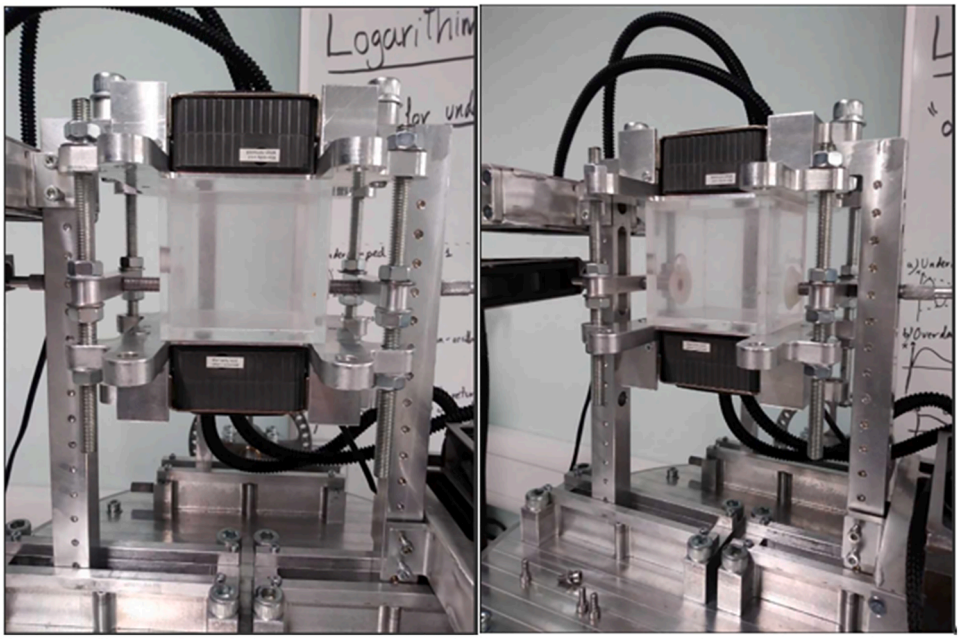

Fig. 2. TCFS Test Rig with the 60 x 60 x 60 mm^3 Perspex FC. Note that the Peltier Brackets, Peltier Devices and associated wiring have been removed for clarity.

it was found that, particularly at temperatures below 70 °C, the PID parameters selected by the controller were insufficiently accurate, thus it is usually necessary to carry out some readjustment of the PID parameters by hand before commencing each experiment. With proper adjustment, a temperature deviation less than +/−0.1 °C, and often as low as +/−0.02 °C, could be achieved. DC pulse signals sent from the Temperature Controller are passed to a Solid State Relay (SSR), which forms a simple series circuit with the Peltier Module (Fig. 3). The SSR essentially translates the sinusoidal output of the Temperature Controller into a square wave 'on-off' signal, therefore modulating the voltage supplied to the Peltier Devices which, in turn, maintains the temperature of the fluid within the FC.

Heat is removed from each Peltier Module by a Cooler Master Seidon 120 V Version 2.0 – this is a liquid-based cooler which pumps a special fluid between a copper plate and a radiator. The power rating, which the Cooling System is designed to operate with, suggests that up to around 300 W may be dissipated by each Cooling System, therefore creating a comfortable factor of safety between the heat dissipated by the Peltier Module and that which can be removed by the Cooling System. Furthermore, the shape of the CSCs is such that they act as extended surfaces, thus aiding with the removal of heat from the Peltier Devices. In this regard, testing has shown that the TCFS Test Rig can reach and maintain a temperature of 100 °C at the outer FC surface without exhibiting any cooling difficulties. At the other end of the spectrum, temperatures as low as 10 °C have been achieved.

The response of the fluid to the applied temperature gradient is recorded by a Digital Microscope (up to 50x zoom) and stored on a nearby PC, whilst a Light Source – a laser with wavelength 532 nm±10 and power max output < 50 mW – is used to illuminate any tracers dispersed in the fluid. The Microscope and Light Source are supported on fully adjustable support mechanisms that allow for 3 planes of motion so that the fluid behavior can be recorded at any position in any of the FCs.

3. Mathematical model

3.1. Geometry

As illustrated in the introduction, fluid convection driven by

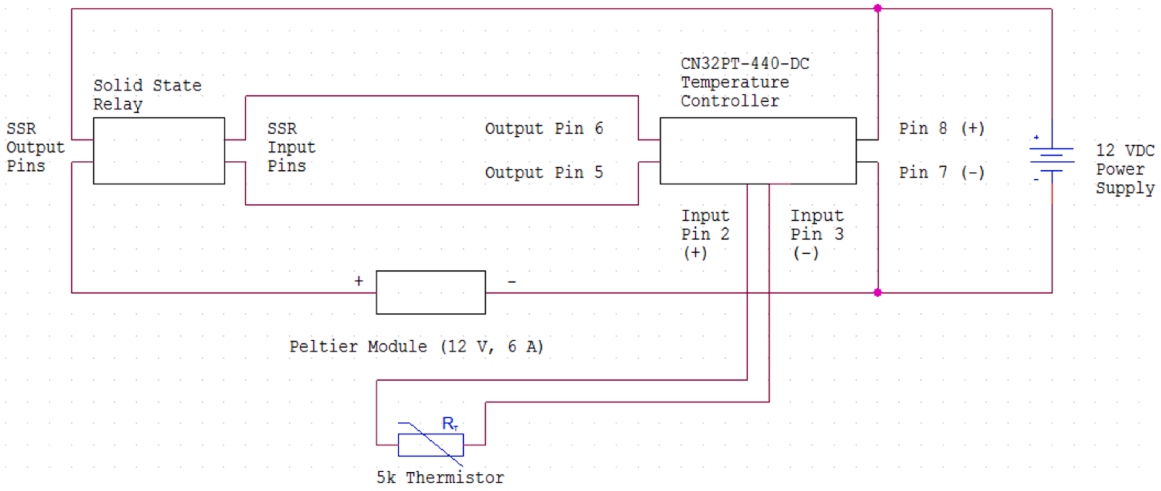

Fig. 3. Circuit Diagram of the Temperature Control Circuit of the TCFS Test Rig. Overall, there are two such circuits i.e. one for each Peltier Device.

buoyancy has been an active topic of both fundamental and applied research over many years; however, despite the considerable effort, a large number of key issues and problems do not seem to have received adequate attention, in particular for what concerns the thermal boundary conditions. These have generally been treated in the framework of standardized models, which, however, may not capture properly some aspects. In turn, these still elude us and are often the source of controversy in the literature.

Modelling the behavior of a fluid system at its boundary is not a trivial task. It may be regarded as the art and craft of defining mathematical relationships, in the form of a single equation or a set of equations, sufficiently involved to represent adequately the physical reality and sufficiently simple to retain those physical aspects only that effectively have an impact on the system behavior.

In numerics, any expression which can be mathematically formulated can be used as a boundary condition and the aforementioned models of purely adiabatic or conducting walls obey the logic of making these conditions as simpler as possible. Resolving the questions relating to the heat loss, however, requires separating different contributions, namely the two stages taken by heat to leave the fluid, the first relating to its *diffusion through the solid walls* and the second associated with *its dispersion in the external ambient*.

Along these lines, in the present work we rely on a more elaborated approach where physical principles and experimental facts are turned into a mathematical and numerical framework by using a multi-domain approach where *fluid and solid regions* are properly coupled in terms of heat exchange. Stripped to its basics, our scheme envisions a portion of fluid encapsulated into a shell of a solid material (perspex) with non-negligible thickness. Moreover, the external boundaries of such a shell are assumed to be in contact with an external gaseous (air) environment at constant temperature T_{amb}. In order to assess the impact of heat losses on the behavior of RB convection, we *intentionally* change the magnitude of the heat flux through the solid walls by modifying the average temperature of the fluid while keeping constant T_{amb}.

The considered configuration is sketched in Fig. 4. It may be regarded as a 'minimal model' in which the fluid is in contact with a solid shell displaying homogeneous and isotropic properties along all directions while heat transfer (controlled or uncontrolled) takes place at its external surface.

3.2. Governing equations

3.2.1. Fluid region

In the liquid region, the classical Navier-Stokes equations for an incompressible fluid hold. These include the balance equations for mass and momentum, to be complemented with the energy equation required for problem closure. In dimensional form, this set can be formulated as:

$$\underline{\nabla}\cdot\underline{V} = 0 \tag{1}$$

$$\rho_0\frac{\partial \underline{V}}{\partial t} + \rho_0\underline{\nabla}\cdot\left[\underline{V}\underline{V}\right] + \underline{\nabla}p = \underline{\nabla}\cdot\left[2\mu\left(\underline{\nabla V}\right)^s\right] + \rho\underline{g} \tag{2}$$

$$\rho_0\frac{\partial (C_v T)}{\partial t} + \rho_0\underline{\nabla}\cdot\left[C_v T\underline{V}\right] = \underline{\nabla}\cdot\left[\lambda^{liquid}\underline{\nabla}T\right] \tag{3}$$

where $\underline{V}$ is the fluid velocity, p is its pressure, T is the temperature, ρ is the liquid density, μ is the dynamic viscosity, λ is the thermal diffusivity, C_v is the specific heat at constant volume, the subscript "0" denotes a reference condition (corresponding to the temperature T_0) and $\left(\underline{\nabla V}\right)^s = \left(\underline{\nabla V} + \underline{\nabla V}^T\right)/2$.

This formulation clearly reflects the initial assumption of constant density, which can be considered as a reliable approximation for a liquid, provided the dependence of density on temperature is properly accounted for in the buoyancy term (the source term at the right-hand side of Eq. (2)). The density appearing there and its dependence on temperature can mathematically be represented with no loss of generality via a Taylor series expansion, i.e.

$$\rho = \rho(T) = \rho(T_0) + \sum_{k=1}^{\infty}\frac{1}{k!}\frac{d^k\rho}{dT^k}|_{T_0}(T-T_0)^k \tag{4}$$

The reader may consider Table 1 for relevant information about the dependence of all the fluid typical properties on temperature for the case of water.

If Eq. (4) is cut after the first-order derivative, i.e. $\frac{d^k\rho}{dT^k}|_{T_0}$ is set to zero for all $k \geq 2$ and the other thermodynamic properties appearing in the balance equations are considered constant (namely, μ, λ and C_v), the overall approach reduces to the so-called Boussinesq framework (see, e.g., [30,31]). Taking into account that for liquids $C_v \cong C_p$ (where C_p is specific heat at constant pressure), the overarching equations for the fluid region can be simplified accordingly as:

$$\underline{\nabla}\cdot\underline{V} = 0 \tag{5}$$

$$\frac{\partial \underline{V}}{\partial t} + \underline{\nabla}\cdot\left[\underline{V}\underline{V}\right] + \frac{1}{\rho_0}\underline{\nabla}p = \nu_0\nabla^2\underline{V} - [\beta_T(T-T_0)]\underline{g} \tag{6}$$

$$\frac{\partial T}{\partial t} + \underline{\nabla}\cdot\left[\underline{V}T\right] = \alpha_0\nabla^2 T \tag{7}$$

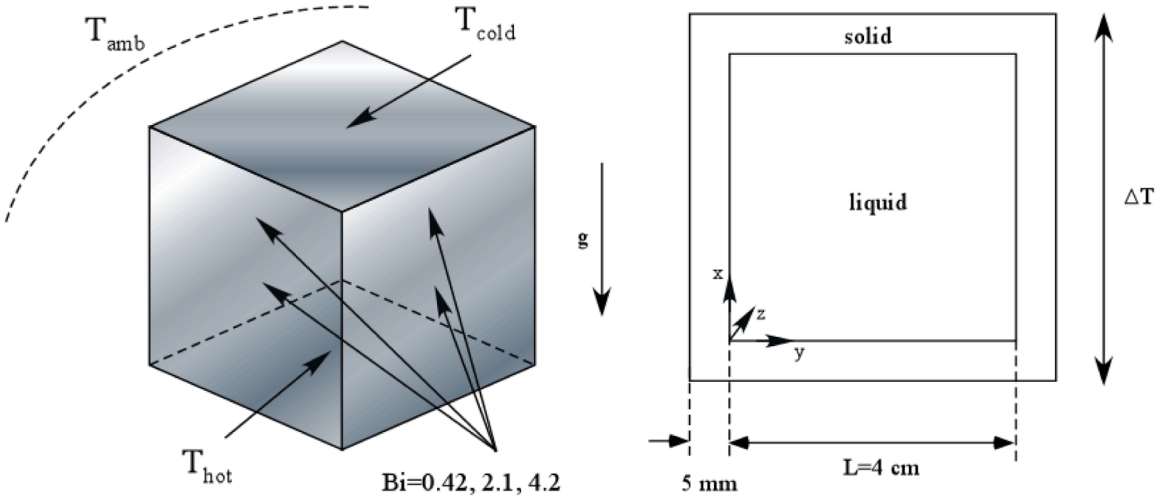

Fig. 4. Geometry of the cavity with the perspec walls and related boundary conditions.

Table 1
Physical properties of water as a function of temperature.

T [°C]	λ [W/(m*K)]	ρ [kg/m^3]	C_p [J/(kg*K)]	μ [kg/(m*s^2)]	ν [m^2/s^2]	α [m^2/s^2]	Pr [/]
10	0.57864	999.77	4192	0.001308	1.3083 10^{-6}	1.3807 10^{-7}	9.4759
20	0.59803	998.29	4182	0.001003	1.0047 10^{-6}	1.4325 10^{-7}	7.0139
30	0.6145	995.71	4178	0.000798	8.0144 10^{-7}	1.4771 10^{-7}	5.4256
40	0.62856	992.25	4179	0.000653	6.5810 10^{-7}	1.5158 10^{-7}	4.3415
50	0.6406	988.02	4181	0.000547	5.5363 10^{-7}	1.5507 10^{-7}	3.5701
60	0.65091	983.13	4185	0.000467	4.7500 10^{-7}	1.5820 10^{-7}	3.0026
70	0.65969	977.63	4190	0.000404	4.1324 10^{-7}	1.6100 10^{-7}	2.5660
80	0.66702	971.60	4196	0.000355	3.6538 10^{-7}	1.6361 10^{-7}	2.2332
90	0.67288	965.06	4205	0.000315	3.2640 10^{-7}	1.6581 10^{-7}	1.9685
100	0.67703	958.05	4216	0.000282	2.9435 10^{-7}	1.6762 10^{-7}	1.7561

where $\rho_0 = \rho(T_0)$and $\beta_T = -\frac{1}{\rho_0}\frac{d\rho}{dT}|_{T_0}$is the well-known thermal expansion coefficient, $\nu=\mu/\rho$ is the kinematic viscosity and α is the fluid thermal diffusivity defined as $\alpha=\lambda/\rho C_p$. Notably, as reported in Gray and Giorgini [32], see Table 2 in their work, in the case of water at atmospheric pressure, the Boussinesq approximation can be considered valid if $\beta_T \Delta T << 1$ (where β_T is of O(10^{-4}), e.g., $\beta_T \cong$ 2.1x10^{-4} 1/K at 20 °C).

3.2.2. Solid region

In the solid region, $\underline{V} = 0$ and the energy equation reduces to the well-known heat diffusion equation:

$$\rho^{solid} C_p^{solid} \frac{\partial T}{\partial t} = \underline{\nabla} \cdot \left[\lambda^{solid} \underline{\nabla} T \right] \tag{8}$$

3.3. Boundary conditions

3.3.1. External boundary of the solid region

On the top and bottom walls of the configuration sketched in Fig. 1 the value of the temperature has been kept fixed; more specifically the bottom has been set as the hotter side at a temperature $T=T_{\rm hot}$ and the top as the colder one at $T=T_{\rm cold}$. On the other walls, the so-called convective heat exchange boundary condition has been implemented as:

$$\lambda^{solid} \frac{\partial T}{\partial n}|_{wall} = -h_{air}(T_{amb} - T_{wall}) \tag{9}$$

where $T_{\rm wall}$ is the temperature of the external boundary of the solid shell and $h^{\rm air}$ is the convective heat transfer coefficient accounting for the heat exchanged due to the natural convection taking place in the external environment. In the present study, an estimation for the order of magnitude of this coefficient has been obtained using available engineering correlations [33] in particular, following [34], we have assumed heat exchange due to natural convection in air with $2 \leq h^{\rm air} < 25$ W/(m^{2}K).

3.3.2. Solid-fluid transition

Where the solid and fluid regions meet the thermal BCs reduce to :

$$\lambda^{solid} \frac{\partial T}{\partial n}|_{solid} = \lambda^{liquid} \frac{\partial T}{\partial n}|_{liquid} \tag{10a}$$

$$T|_{solid} = T|_{liquid} \tag{10b}$$

which express the continuity of heat flux and temperature, respectively; the reader is referred to Table 2 for relevant information about the physical properties of perspex.

Table 2
Physical properties of perspex.

ρ	C_p	λ
[kg/m^3]	[J/(kgK)]	[W/(mK)]
1190	1459	0.19

3.4. Non-dimensional parameters

Putting the problem is non-dimensional form is beneficial as it leads to a shrinkage of the number of parameters potentially affecting the dynamics. Such strategy formally yields a limited set of influential non-dimensional numbers:

$$\mathrm{Pr} = \frac{\nu}{\alpha} \ (Prandtl\ number) \tag{11}$$

$$Ra = \frac{g\beta_T \Delta T L^3}{\nu\alpha} \ (Rayleigh\ number) \tag{12}$$

$$Bi = \frac{h_{air} L}{\lambda^{solid}} \ (Biot\ number) \tag{13}$$

in the present work all the reference physical properties appearing in these numbers have been evaluated for $T_0=T_{\rm cold}$. Moreover, the ΔT appearing in the definition of the Rayleigh number is formally the difference between $T_{\rm hot}$ and $T_{\rm cold}$, i.e. the temperature actively controlled (kept constant) at the two opposing *external* sides of the solid shell. This means that this ΔT should not be confused with the jump of temperature ΔT_{eff} effectively created in the fluid, which differs from ΔT due to the presence of a region of solid material located between the surface where the temperature is actively controlled and the internal liquid. Accordingly, we also introduce a variant of the Rayleigh number based on ΔT_{eff}, namely, $Ra_{eff} = \frac{g\beta_T \Delta T_{eff} L^3}{\nu\alpha}$ where ΔT_{eff} is defined as the difference between the average temperatures on the internal walls corresponding to the externally heated and cooled surfaces, respectively, and it is therefore only a fraction of the imposed temperature jump, i.e. $Ra_{\rm eff} < Ra$.

3.5. The numerical method

The set of governing equations has been integrated in the framework of the PISO (Pressure Implicit Split Operator) method originally elaborated by Issa [35] and freely available as a time-marching native solver through the OpenFoam computational platform [36]. In OpenFoam such algorithm is implemented as a collocated grid approach, i.e. all the variables are defined in the center of the cells and, accordingly, the [37] scheme is exploited to achieve good coupling of velocity and pressure (i.e. through dedicated interpolation of the velocity nodal values).

In particular, the simulations have been conducted using the chtMultiRegionFoam solver (OpenFOAM Version 4.1). For what concerns the discretization of the equations, we have selected a second order central difference scheme for both the convective and diffusion terms, and a Preconditioned Bi-Conjugate Gradient (PBiCG) to solve the resulting system of algebraic equations with an Incomplete Lower Upper (DILU) preconditioner being applied for velocity and temperature in the predictor step. The elliptic equation for the pressure has been iteratively solved in the frame of a Generalized Geometric-Algebraic Multi-Grid (GAMG) method [36]. This approach has already proved its ability to capture the dynamics of interest in similar situations (see, e.g., [38]).

3.6. Validation and mesh independence study

In this section, the proper mesh size is assessed on the basis of a parametric study relying on the evaluation of a sensitive quantity, that is, the frequency of oscillation for time-periodic convection. For simplicity, a classical Rayleigh–Bénard configuration with perfectly adiabatic walls is considered. Moreover, the study is carried out in the framework of the Boussinesq approximation (Eqs. (5)-(7)). The considered Prandtl number is Pr=6.9 and the Rayleigh number is $Ra = 4.4 \times 10^5$. This value corresponds to a ΔT=0.5 C°, representative of the ΔT_{eff} established in most of the present experiments for which an oscillatory pattern was found. As shown in Table 3, three (uniform) mesh resolutions have been considered: 60×60, 100×100, 150×150.

As made evident by this table, a uniform mesh with resolution 100×100 makes the relative variation with respect to the previous resolution ≅ 0.1 %. If the Rayleigh number is increased to 10^6, the flow becomes turbulent. Even in this case, however, a grid 100 x 100 is sufficient to make the main properties of the flow mesh-independent, as witnessed by the maximum frequency and related amplitude reported in Table 4. Accordingly, we have used this resolution for all the simulations considered in the present work.

Tables 5 and 6 finally demonstrate the reliability of the present numerical approach through comparison with well-established results in the literature.

4. Results

In this section, we describe the results obtained via solution of Eqs. (1-3) and (8)-10 showing that in this framework, progression towards fully developed chaos is mediated by the existence of *multiples solutions* and switches from the classical Ruelle-Takens scenario to the alternate Curry-Yorke route. In particular, for each case, results are discussed following a peculiar order of presentation, which reflects our intention to implement a precise analysis hierarchy, by which the degree of complexity of the problem is progressively increased (i.e. *2D computations→Experiments→3D simulations*).

All the cases presented in this section refer to the fluid (water) encapsulated into the shell of perspex material (with inner dimension 4 x 10^{-2} m as indicated in Sect. 2) and properties depending on temperature as illustrated in Sect. 3.2.1. Different possible values are considered for T_{cold}, namely, 20, 40 and 60 °C for a fixed $T_{\text{amb}} = 22$ °C. As outlined at the end of Sect. 3.4, we report the "nominal" Rayleigh number (Ra) (see Eq. (12)) together with the "effective" Rayleigh number (Ra_{eff}), the latter being defined using the mean temperature of the hot and cold side of the *internal side* of the shell (in contact with the fluid) and related difference. Notably, since the temperature on these sides is free to vary, Ra_{eff} can also take negative values; in particular, as shown in Table 7 this happens when the average temperature of top side is greater than that evaluated at the bottom side.

Cross comparison of Tables 7 and 8 also indicates that the Rayleigh number computed according to its standard definition (Eq. (12)) can take different values for a fixed value of ΔT at different values of T_{cold} due to the different values of the fluid physical properties used to calculate it.

Table 3
Non-dimensional angular frequency (ω) as a function of mesh size (Pr=6.9, $Ra = 4.4 \times 10^5$, time-periodic flow).

Mesh	ω	Variation [%]
60×60	332.366	0.556
100×100	334.225	0.125
150×150	334.644	/

Table 4
Maximum non-dimensional angular frequency present in the frequency spectrum ω and related amplitude as a function of mesh size (Pr=6.9, $Ra = 10^6$, turbulent flow).

Mesh	ω	Variation [%]	Ampl.	Variation [%]
100×100	439.6		46.44	
150×150	435.2	1.011	47.55	2.334

Table 5
$A = 1$, Ra=10^5, Pr=0.71. Comparison with Table 2 of Ouertatani et al. [39], mesh 128×128. Velocity scaled with u_0=sqrt(gβHΔT).

Quantity	Present	Ouertatani et al. [39]
U_{max}	0.3443	0.3442
V_{max}	0.3754	0.3756
Nu_h	3.9204	3.9097

Table 6
$A = 4$, Ra=10,000, Pr=0.71. Comparison with Table 3 of Ouertatani et al. [39] and Table 2 of Soong et al. [40].

Nusselt number	Present	Ouertatani et al. [39]	Soong et al. [41]
Nu_h	2.53163	2.52523	2.52234
Nu_c	2.53164	2.52525	2.52243

Table 7
Ra and Ra_{eff} at different ΔT. $T_{\text{cold}} = 60$ °C, Bi=4.2 ($h = 20$ W/m^{2}K).

ΔT [°C]	Ra	Ra_{eff}
5	2.18×10^7	-6.068×10^6
9	3.93×10^7	-4.614×10^6
12	5.24×10^7	-2.336×10^6

Table 8
Ra and Ra_{eff} at different ΔT. $T_{\text{cold}} = 40$ °C, Bi=2.1 ($h = 10$ W/m^{2}K).

ΔT [°C]	Ra	Ra_{eff}
6.6	1.61×10^7	7.092×10^5
8	1.95×10^7	1.021×10^6
12	2.92×10^7	1.914×10^6

4.1. Two-dimensional simulations

As anticipated, first we discuss results obtained in the framework of 2D simulations. Notably, given the reduced computational weight of numerical simulations carried out under the constraint of 2D flow, we could perform a wider spectrum analysis considering more extended ranges of the imposed ΔT and Biot number.

Along these lines, we wish also to highlight that preliminary critical discussion of the existing literature on the subject may be considered instrumental in discerning the peculiar aspects of the problem considered here via cross-comparison and identification of differences with already studied cases, i.e. the canonical configurations with adiabatic or conducting walls.

For the two-dimensional case, it is well known that, when the abovementioned classical boundary conditions are considered, several modes of the most dangerous perturbation exist, which can replace each other when the cavity aspect ratio A is varied. As an example, seminal studies about RB convection in cavities with various aspect ratios for adiabatic and conducting walls are due to [41] and [42], respectively. The study for adiabatic walls was further refined by [22], while the reader may consider [24] and [43] for valuable information about the *possible symmetries of the emerging flow*.

Indeed, the possible patterns formed by RB convection in a square

cavity can, in general, be predicted by considering various combinations of the possible symmetries along the horizontal and vertical directions. In simple terms, owing to the symmetry/antisymmetry of the governing equations and of the boundary conditions, the allowed patterns can be obtained by reflection about the vertical cavity centerline (parallel to the applied temperature gradient), about the horizontal cavity centerline (perpendicular to the gradient) and about both of them. This naturally leads to the identification of four possible cases, as illustrated in Fig. 5.

As shown in this figure, the modes differ essentially in the number of rolls along the horizontal and the vertical directions. If the number of vortex cells along both the horizontal and the vertical directions is odd, the resulting pattern pertains to the family of antisymmetric-antisymmetric (aa) modes. Vice versa, if it is odd, a symmetric-symmetric (ss) mode is obtained. Different combinations result in the symmetric-antisymmetric (sa) and antisymmetric-symmetric (as) modes, respectively; these display an even number of rolls along the horizontal direction and an odd number of cells in the perpendicular direction and vice versa, respectively. In practice, different modes can be selected depending on the considered value of the Rayleigh number and the thermal boundary conditions. At relatively high values of the Rayleigh number, i.e. relatively far from the threshold for the onset of convection from the initially thermally diffusive quiescent state, it is known that initial modes with the (aa) or (sa) symmetries can even produce modes with different symmetries via a nonlinear interaction mechanism; as an example, this was shown by [44] for the case of conducting sidewalls. If the initial mode has the (aa) symmetry,in particular, the (ss) mode is excited; the thermal convection arising in such a case after a flow bifurcation can be expressed as a combination of these two modes. If the initial mode has the (sa) symmetry, the aforementioned nonlinear interaction can produce all the four possible modes (aa, sa, as and ss); in such a case the flow exhibits no symmetry [44].

Given these premises, it is worth starting the description of the present results from the simple realization that the heat exchanged with the external environment and the effective distribution of temperature established inside the shell of solid material that encapsulates the liquid can obviously interfere with the selection of modes with these symmetries and therefore cause significant changes in the typical bifurcation hierarchy of RB flow under the constraint of two-dimensionality.

In particular, first we present the case with T_{cold}= 60 °C for which the most interesting dynamics have been obtained.

As shown in Fig. 6, for this specific configuration we have found the 2D flow to undergo a Hopf bifurcation, which is not present in analogous simulations conducted assuming the classical adiabatic conditions. For $Ra<Ra_{cr}$, interestingly, the heat exchanged to the ambient through the lateral walls forces the flow to develop a single thermal plume located approximately in the center of the cavity, with hot fluid rising at the center, and fluid cooled due to heat loss sinking close to the lateral walls, see Fig. 6a and 6b. The threshold for this instability depends strongly on the heat exchanged and increases as the Biot number becomes higher (Fig. 6c).

For Bi=0.42, corresponding to a convective heat exchange coefficient of h = 2 W/(m^{2}K) for the container described in Sect. 2, the initially steady flow becomes time-periodic between $\Delta T = 2.6$ and 2.7 K ($1.131\times10^7 < Ra < 1.175\times10^7$); in these cases, a single-frequency state with a plume displaying a pulsating behavior in the vertical direction is attained; between $\Delta T = 2.7$ and 2.8 K ($1.175\times10^7 < Ra < 1.218\times10^7$) a second Hopf bifurcation occurs, leading the system to a quasi-periodic state where a plume wobbling mechanism with a lower frequency is superimposed on the pulsating one. These two fundamental modes of oscillation are illustrated in Fig. 7 by means of four snapshots evenly distributed in one period of oscillation: the first row represent the high frequency pulsating phenomenon and the second row the low frequency wobbling. In the second row, the first high frequency has been filtered out, leaving only the smaller one. The reader is also referred to Fig. 8 for a map of the overall system evolution as a function of the Rayleigh number.

The related velocity signals and frequency spectra are reported as a function of ΔT in Fig. 9. As witnessed by this figure, there is a periodic regime where only one frequency, related to the pulsating mechanism in the vertical direction, exists. As a value of $\Delta T \cong$ 2.8 K (Ra=1.218×10^7) is exceeded, a second Hopf bifurcation occurs and the wobbling mechanism is turned on. Finally, on increasing ΔT beyond 3 K (Ra=1.305×10^7), a chaotic regime is developed; the reader is expressly referred to the spectra shown on the right of this figure to get additional insights into these processes. In particular, it can be seen that transition to chaos essentially follows the so-called Ruelle-Takens-Newhouse path (Newhouse et al. [45]), where a third Hopf bifurcation is allowed to turn a T^2 torus into a T^3 torus before a fully chaotic state is developed (Fig. 10).

To support this statement, we have also evaluated the so-called 'correlation dimension' D [46-50]) and plotted it as function of ΔT in Fig. 11. By inspecting this figure, it can be seen that the system jumps from a value of the correlation dimension ≅ 2 to another value ≅ 3, while there are no points in the intermediate range. This clearly indicates that, as envisaged by the Ruelle-Takens-Newhouse scenario, chaos and fractalization ($D > 3$) occur only after a T^3 torus is formed. Moreover, another interesting aspect is evident in this figure: when such a threshold is exceeded, the correlation dimension does not increase smoothly with the control parameter ΔT. Rather a transition region exists between $\Delta T = 3$ and 3.2 K ($1.218\times10^7 < Ra < 1.392\times10^7$) where the system suddenly jumps from $D = 3$ to a state with higher degree of chaos.

Continuing with the description of the results obtained under the constraint of two-dimensionality, it is also worth recalling that the Biot number obviously plays a role in such dynamics. As an example, for Bi=2.1, we found quite a different evolutionary path.

More precisely, we have observed the wobbling instability only. Since the transition to chaos follows the same route already discussed for Bi=0.42, however, this case is no longer described here. Rather we concentrate on Bi=4.2.

Most interestingly, for this value of the Biot number, we have found *two different branches of solutions, which coexist in the phase space*. The first is a wobbling state similar to that already discussed before, consisting of a plume that undergoes a time-dependent behavior with its stem remaining aligned with the direction of gravity; the second is an asymmetric pulsating plume, which differently from the behavior shown

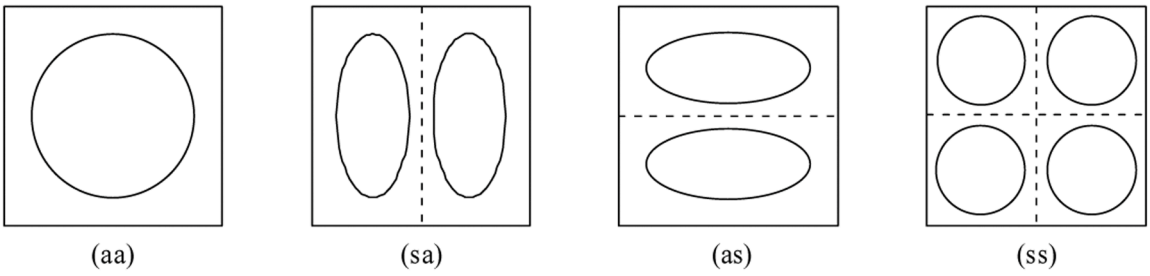

Fig. 5. Categorization of possible solutions of RB convection in 2D finite enclosures in terms of related symmetries.

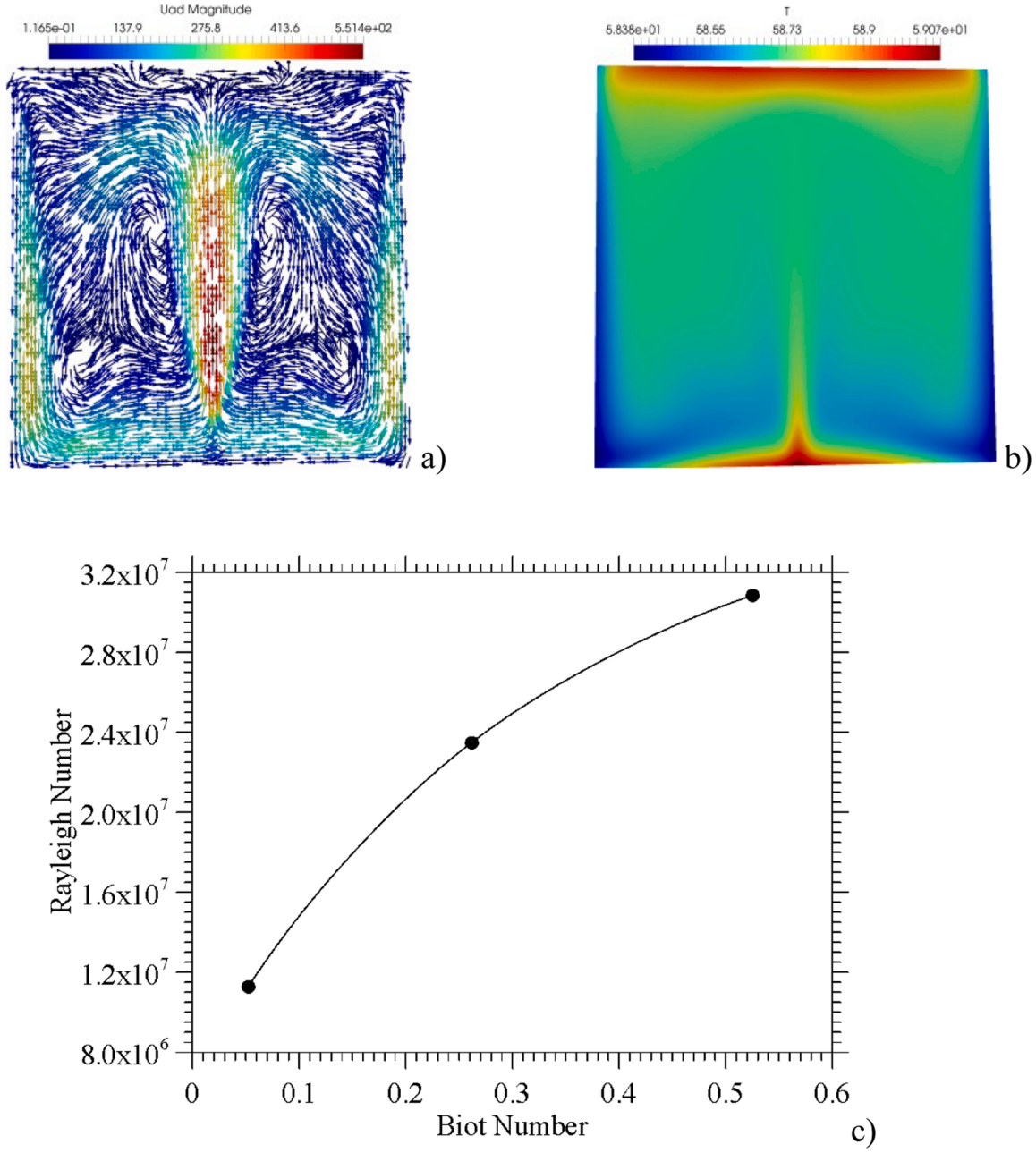

Fig. 6. Velocity field (a) and (b) temperature distribution for $\Delta T = 2$ K, $T_{cold} = 60$ °C (Ra=8.7×10^6, Ra_{eff}=−4.165×10^5) and Bi=0.42, (c) First oscillatory instability threshold as function of the Biot number (the spline is used to guide the eye).

in Fig. 7, has the plume stem bended left or right, these two possible solutions being one the mirror image of the other.

The corresponding non-dimensional frequencies are reported in Fig. 12 as a function of Ra. It can be seen that between $Ra \cong 3.1\times10^7$ and $Ra \cong 4.1\times10^7$ ($\Delta T = 7$ and 9.5 K) these two mechanisms coexist as *multiple solutions*, i.e. as states that can be chosen by the system *starting from different initial conditions*. Most interestingly, the route to chaos follows a different scenario with respect to that reported in Fig. 11: the system undergoes a first Hopf bifurcation from the initial steady state at $\Delta T = 6.1$ K for the pulsating instability and at 7.1 K for the wobbling one. On further increasing the temperature difference, both solutions (illustrated in Fig. 13) are subjected to a second Hopf bifurcation, leading the attractor to become a T^2 torus. Immediately after this second bifurcation, the T^2 attractor suddenly loses its stability and evolves into a chaotic state without passing through the intermediate stage of a T^3.

At this stage, towards the end to put these somehow unexpected results for Bi=4.2 in a more general theoretical context, it is worth considering analogous findings obtained by other authors over the years for situations with canonical thermal boundary conditions. A broad outline can be elaborated as follows. For low-Pr fluids (e.g., liquid metals) the so-called period doubling (Feigenbaum) scenario has often been reported in past studies (e.g. [51,52]). For higher Prandtl numbers (like water), however, the situation is more complex owing to the existence of several mechanisms that can compete in determining the transition from an initial steady state to time-dependent conditions (a classical example of this complexity being represented by the aforementioned Busse balloon). For containers with aspect ratio close to 1 as that considered in the present work, [53] observed two different routes to chaos: the Feigenbaum scenario and the Ruelle-Takens-Newhouse evolutionary path. In particular, the latter has been found to be

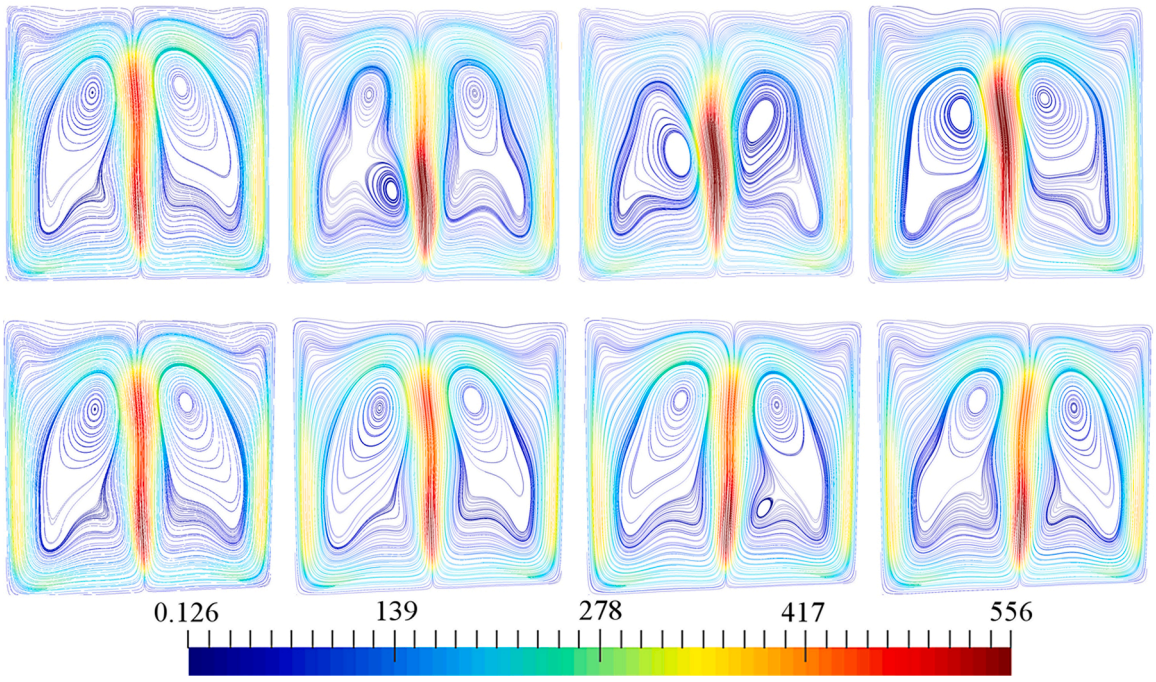

Fig. 7. Four snapshots evenly distributed in one period of oscillation of velocity (non-dimensional) magnitude for ΔT = 2.9 K, T_{cold} = 60 °C (Ra = 1.26×10^7, Ra_{eff}=3.186×10^5) and Bi=0.42 (h = 2 W/(m^{2}K)). First row plume pulsating phenomenon. Second row: wobbling instability with a lower frequency.

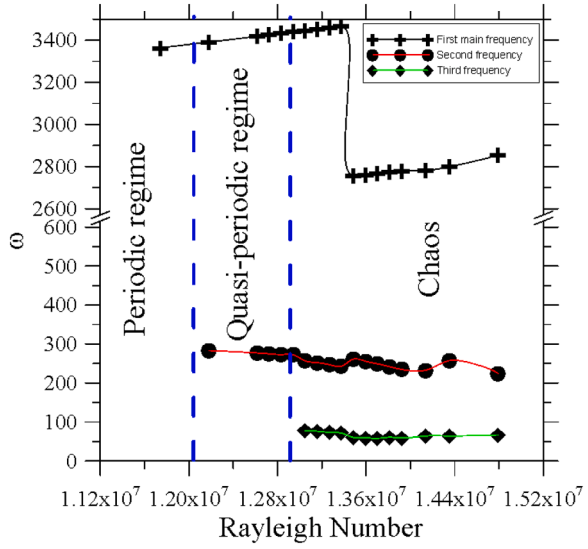

Fig. 8. Non-dimensional angular frequency (ω) as a function of the Rayleigh number for the cases with T_{cold} = 60 °C and Bi=0.42 (h = 2 W/(m^{2}K)).

relatively recurrent in RB convection, especially for high-Pr fluids [54,51]).

Like other fluid systems with uniform heating from below (see, e.g., [55]), Rayleigh–Bénard convection, however, can also undergo the so-called 'attractor crises' [56]. As discussed by [57], these crises arise when *a collision occurs between an unstable periodic orbit and a coexisting chaotic attractor*. A crisis typically leads to sudden phenomena such as the creation, the destruction or a change in the size of a chaotic attractor. Moreover, it is known that three types of crises are possible, generally referred to as 'boundary' (or 'exterior') crisis, 'interior' crisis and 'attractor merging'. In the light of these arguments, a very interesting interpretation can be elaborated for our findings relating to the conditions Bi=4.2 and T_{cold}=60 °C, for which the two possible oscillatory instabilities have been depicted in Fig. 13.

For this case, as discussed in the preceding text, three stable attractors exist in the phase space, one pertaining to the symmetric wobbling instability and other two belonging to the non-symmetric pulsating one, whose manifestation in the physical space is a plume with distorted shape inclined to the left or to the right, the two states being one the mirror image of the other. In line with similar findings reported in other circumstances (the reader being referred, e.g., to [58,55]), we argue that the interplay among these attractors is responsible for the crisis determining the sudden transition from the T^2 torus to high-dimensional chaos.

Interestingly, along the non-symmetric pulsating branch (blue line in Fig. 12) a "symmetry recovery crisis" occurs at $\Delta T\cong$ 9.5 K due to interaction between the two spatially distorted possible pulsating solutions. The new emerging state yet oscillates in a chaotic fashion, but the spatial symmetry of the rising plume is now 'central' on average, i.e. it wobbles and pulsates about the center of the cavity by jumping continuously from a non-symmetric solution to the other as shown in Fig. 14. Following the wobbling branch (red line in Fig. 12), a boundary crisis occurs at $\Delta T\cong$ 12.5 K; in particular, after undergoing a bifurcation to a T^2 state, this solution loses definitely its stability giving rise to a spatio-temporal behavior similar to that illustrated in Fig. 14.

These evolutionary paths may be regarded as realizations of the Curry-Yorke scenario [59], which, as also shown in other works [55,60], seems to be a typical feature of systems with multiple solutions.

For the specific case of time-dependent 2D RB convection, other interesting numerical results for classical adiabatic or conducting sidewalls are also available in the literature. Most interestingly, [23] could predict complex flow patterns and textural transitions in both non-chaotic and chaotic flow regimes together with multistability (see also [26]). According to their study, for Pr= 6.8, aperiodic (chaotic) flows of non-integer dimension like those reported here occur. Moreover, roll merging and separation were found to be an important feature of the dynamics; in some cases corner rolls were observed to migrate into the interior of the cell and to grow into regular rolls; with large rolls shrinking and retreating into corners.

The most striking difference with respect to the present findings

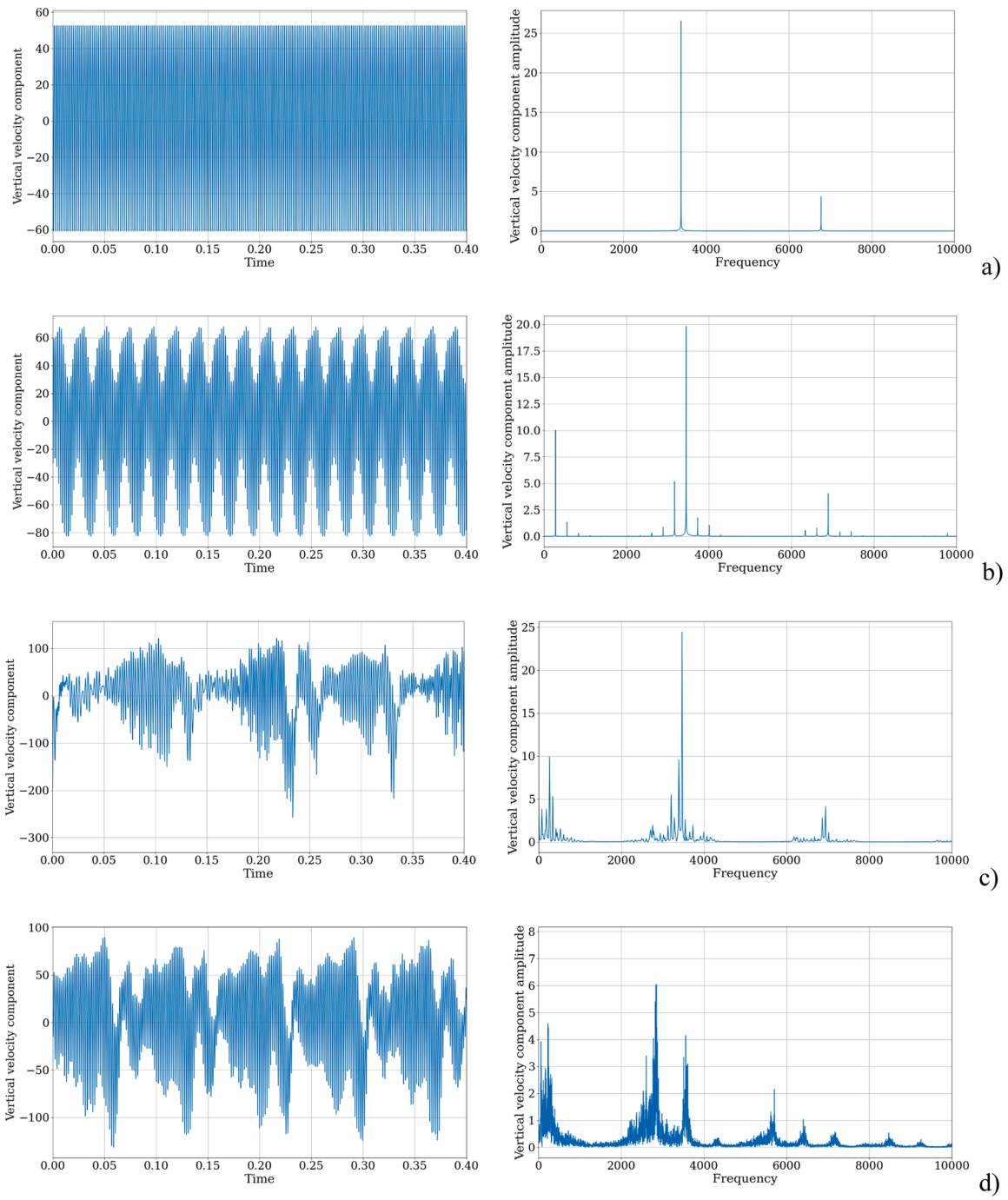

Fig. 9. Time series (left) and related frequency spectra (right) at $x = 3/4$ and $y = 1/2$ ($T_{cold} = 60$ °C and Bi=0.42); a) ΔT=2.7 K, Ra=1.175×10^7, (Ra_{eff}=1.707×10^5); b) ΔT=2.975 K, Ra=1.294×10^7, (Ra_{eff}=3.73×10^5); c) ΔT=3.0 K, Ra=1.305×10^7, (Ra_{eff}=3.730×10^5); d) ΔT=3.4 K, Ra=1.479×10^7 (Ra_{eff}=6.23×10^5).

relates to the 'symmetry' of emerging convection. As the reader will easily realize by visual inspection of Figs. 6, 7, 13 and 14, regardless of the values of the Rayleigh number, the heat loss occurring through the lateral walls of the square cavity essentially forces convection to take the (sa) structure, which corresponds to the presence of a central plume. It also limits the complexity in terms of patterning behavior as no growing or shrinking vortices like those found by [23] or [26] have been detected in the present case.

Perhaps, most interestingly, widespread preference for the (sa) symmetry is responsible for the trend shown in Table 7, i.e. the negative values being taken by Ra_{eff}. The fluid descending close to the lateral walls exchanges heat with them and reaches the bottom being colder, causing a drop in the temperature of the internal side of the bottom wall. This phenomenon is more pronounced when Bi on the lateral walls is high and when T_{cold} and T_{hot} are much higher than T_{amb}.

Having completed a sketch of the situation with T_{cold}=60 °C, we turn now to examine the other cases for which the average temperature of the cavity is smaller.

For T_{cold}=40 °C, Bi=0.42 (h = 2 W/(m^{2}K)), the flow exhibits a steady, bi-cellular and symmetric pattern, with a central rising plume until a value of ΔT = 2.9 K (Ra=7.01×10^6) is reached. After such a threshold, the flow becomes oscillatory with a central wobbling plume (Fig. 15a). If the temperature is further increased, the pattern takes a non-symmetric configuration with the average position of the central

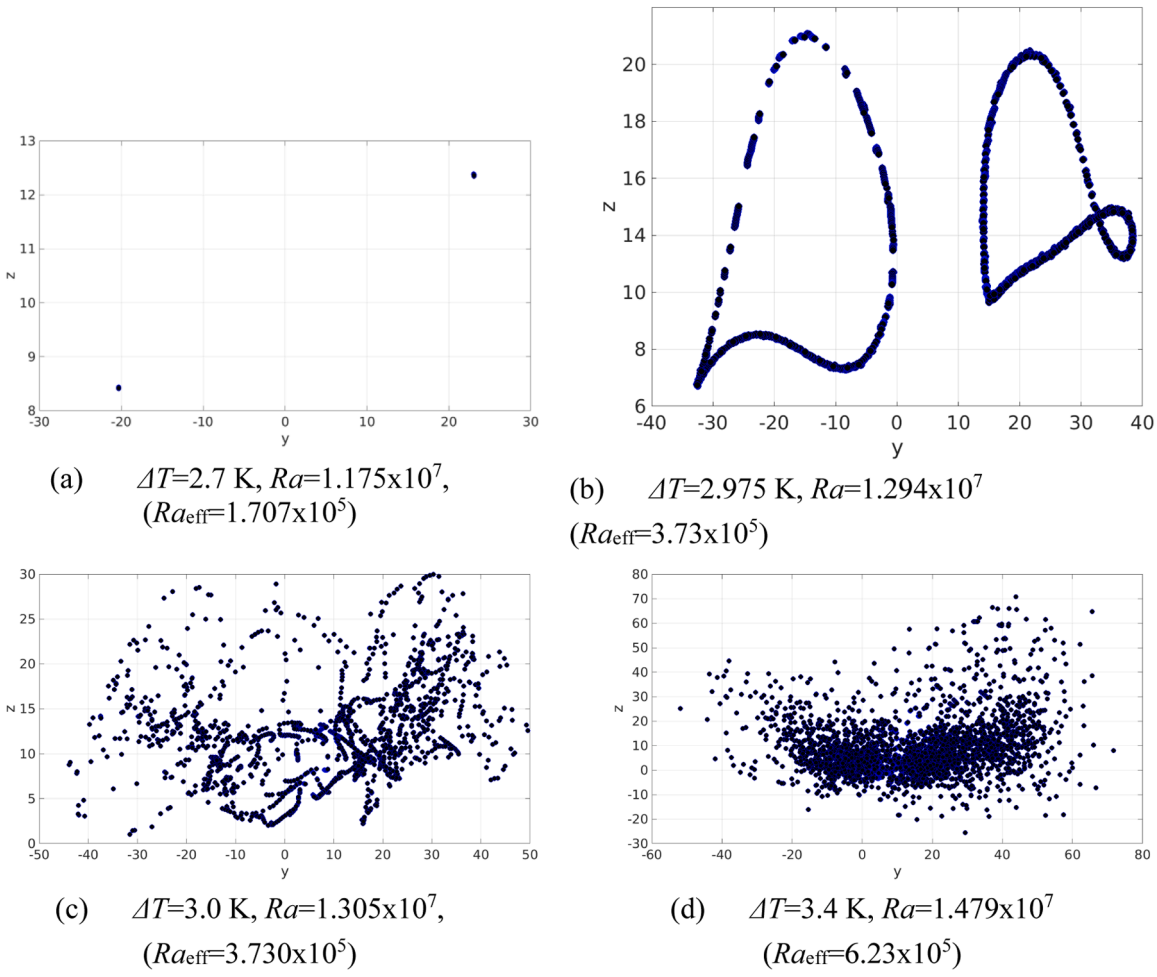

Fig. 10. Poincaré sections of the attractor in the embedded space at constant x in the middle of the attractor (T_{cold} = 60 °C and Bi=0.42).

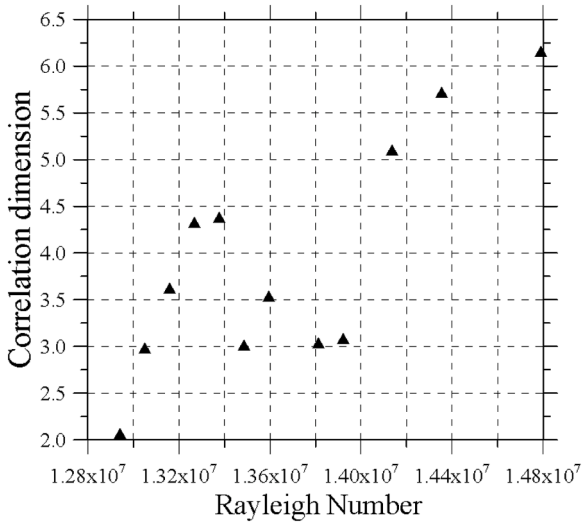

Fig. 11. Correlation dimension as a function of the Rayleigh number for Bi=0.42 and T_{cold}=60 °C.

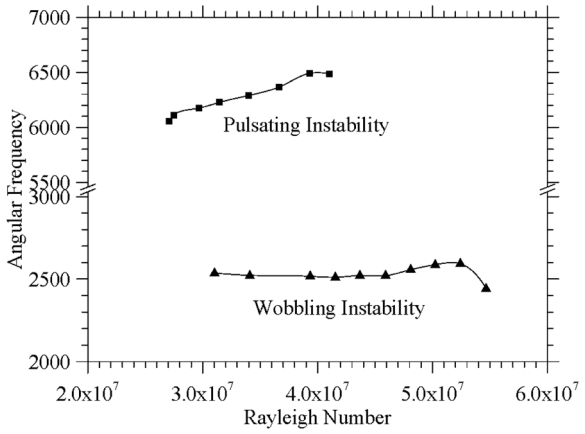

Fig. 12. Main angular frequency (ω) as function of *Ra*. T_{cold} = 60 °C and Bi=0.42.

plume shifting to the left or to the right (Fig. 15b); this gives rise again to two branches of possible non-symmetric solutions.

On increasing Bi, (T_{cold}=40 °C, Bi=2.1), the flow becomes oscillatory between ΔT = 6.4 and 6.5 K ($1.56\times10^7 < Ra < 1.58\times10^7$) with a pulsating instability and a central rising plume very similar to that already discussed for T_{cold} = 60 °C. As evident in Table 8, for this case (T_{cold}=40 °C), only positive values are possible for Ra_{eff}, which confirm the trends highlighted before, i.e. that when the T_{cold} and Bi are high, the Ra_{eff} can be much smaller than *Ra* or even take negative values. The value of Ra_{eff}, indeed, increases when the heat exchange through the lateral walls is reduced: from the negative values of the Table 7 we obtain the positive ones of Table 8 by decreasing both Bi and T_{cold} .

On increasing ΔT, the flow enters a quasi-periodic regime at $\Delta T \cong$ 6.8

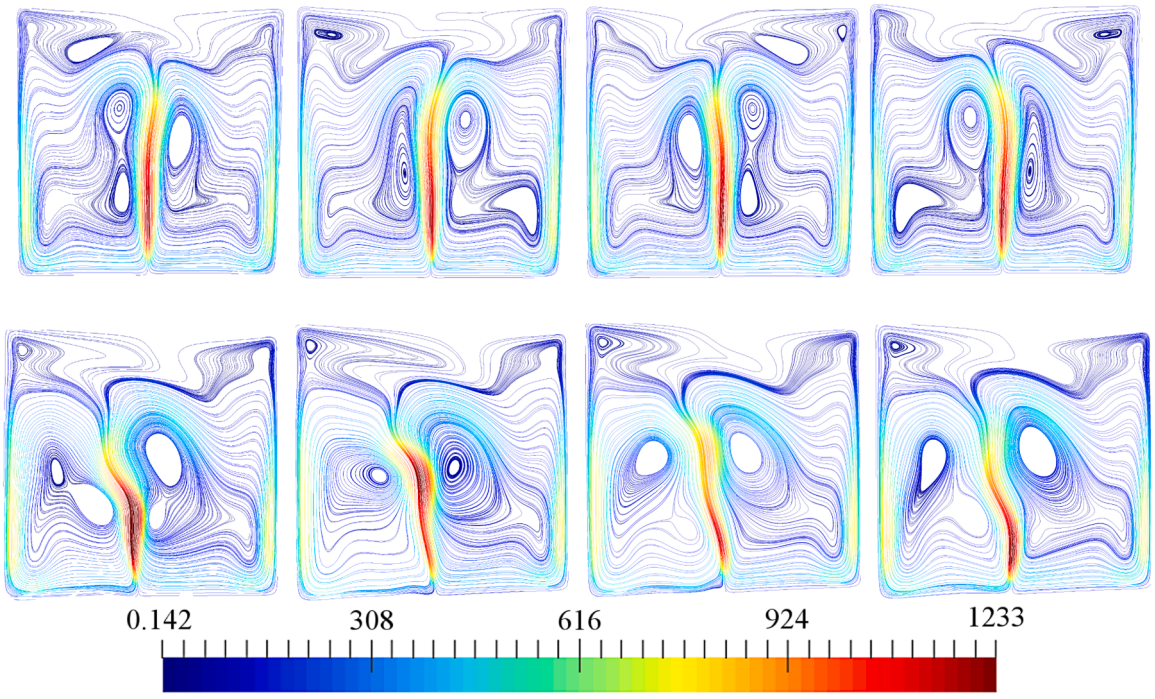

Fig. 13. Snapshots of velocity field (non-dimensional amplitude) for Bi=4.2, T_{cold}=60 °C, Ra=3.93×10^7: First row: the wobbling symmetric instability (mirror symmetry with respect to the midsection preserved). Second row: non-symmetric pulsating mechanism (mirror symmetry with respect to the midsection is broken).

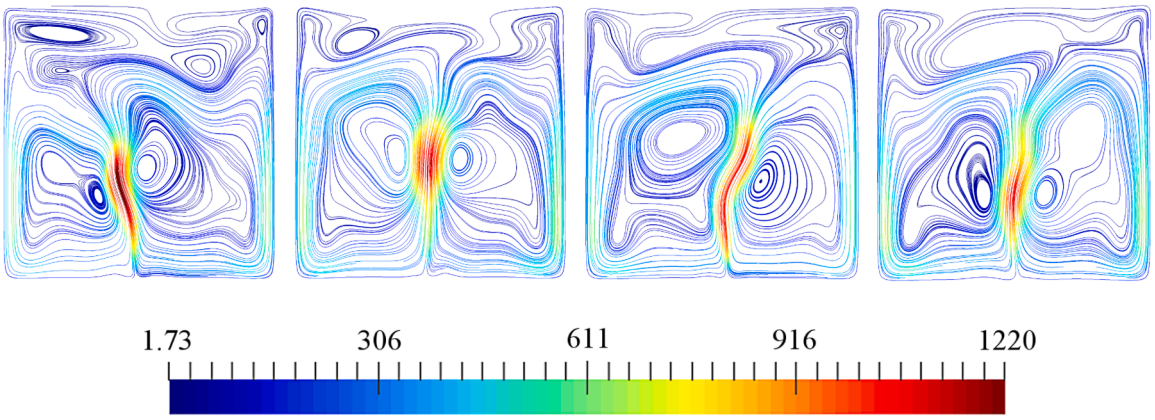

Fig. 14. Snapshots (nondimensional velocity amplitude) of chaotic pattern due to the interaction of the two non-symmetric solutions. Bi=4.2, T_{cold}=60 °C, Ra=4.15×10^7.

K (Ra=1.65×10^7, Fig. 16). In this regime a new wobbling mechanism is superimposed on the previous one, giving rise to a hybrid oscillatory state. Unlike the situation with T_{cold} = 60 °C and Bi=0.42 (h = 2 W/(m^{2}K)), unfortunately, in this case we could not estimate the correlation dimensions due to the very high-dimensional nature of the emerging chaos (for which the classical [49,50] is no longer applicable, see, e.g., [61]).

4.2. Experimental results

All the experiments have been conducted using the facility and fluid containers described in Sect. 2 with an ambient temperature ≅ 22 °C and imposed ΔT fixed to 20 K. In particular, the experimental results for T_{cold} = 60 °C and T_{cold} = 20 °C are summarized in Figs. 17 and 18, respectively. For each case, the velocity as a function of time, measured at a fixed position and some snapshots of the velocity field are reported. In particular, the vector plots result from the application of a PIV (Particle Image Velocimetry) technique to experimental videos providing the evolution in time of tracer particles (size 50 μm made visible by a light cut).

As the reader will realize by comparing such figures (e.g., Fig. 17) with the complex scenario unveiled on the basis of numerical simulations carried out under the constraint of two-dimensional flow, the 3D flow is much more stable. More specifically, as evident in Fig. 17c, a time-periodic flow is obtained for T_{cold} = 60 °C, ΔT = 20 K, Ra=8.7×10^7. As discussed in Sect. 4.1, for the same conditions (see Figs. 7-14), the equivalent 2D states would essentially be chaotic owing to the gradual corrugation of a T^2 torus (Curry-Yorke scenario) or the sudden transition to chaos originating from a T^3 torus (Ruelle-Takens route).

Moreover, comparison of the experimental results for two different values of T_{cold} (namely cross-comparison of Figs. 17 and 18) is also particularly instructive as it reveals that *a larger average temperature of the system can produce a significant simplification in the frequency spectrum*

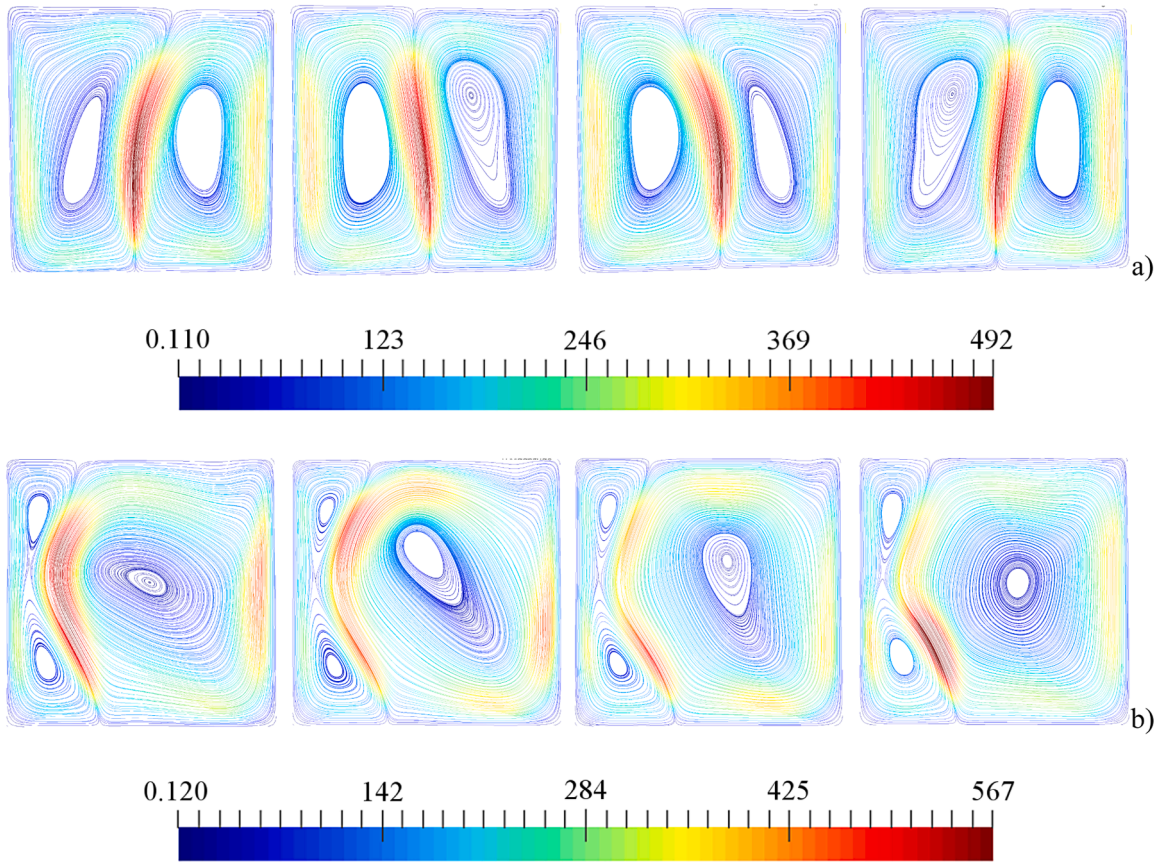

Fig. 15. a) Four snapshots of velocity field evenly distributed along one period of oscillation for ΔT=3 K, T_{cold} = 40 °C (Ra=7.06×10^6, Ra_{eff}=5.874×10^5) and Bi=0.42 (h = 2 W/m^{2}K), wobbling instability with central plume. b) Four snapshots of velocity field evenly distributed along one period of oscillation for ΔT=4.5 K (Ra=1.06×10^7, Ra_{eff}=9.754×10^5) and Bi=0.42 (h = 2 W/m^{2}K), unstable flow configuration with the average position of the central plume shifting to the left or to the right.

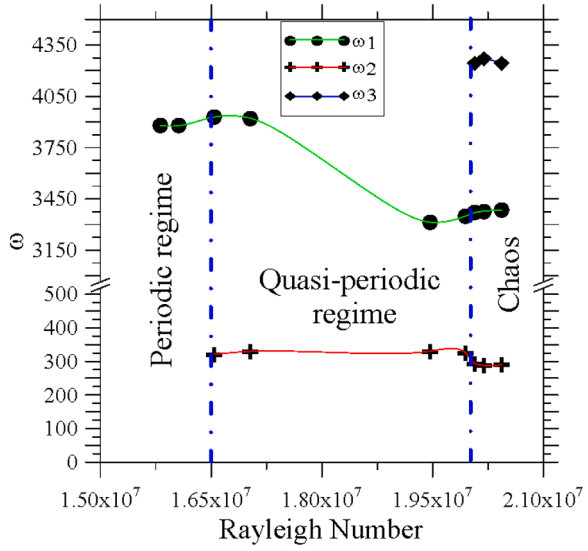

Fig. 16. Frequencies as a function of Rayleigh number. T_{cold} = 40 °C, Bi=2.1 (h = 10 W/(m^{2}K)).

and in the flow patterning behavior.

We ascribe this stabilization to the heat transfer occurring through the walls perpendicular to the z axis, which contribute (together with the other two non-thermally controlled walls) to extract energy from the system.

Moreover, as made evident by further visual inspection of these figures, an increase in the average temperature of the fluid while keeping fixed the imposed temperature difference has a two-fold effect. Apart from determining a transition from the non-time periodic signal visible in Fig. 18c to the time-periodic state represented by the signal reported in Fig. 17c, the increased heat transfer towards the ambient also causes remarkable changes in the structure of the flow.

Following up on the previous point, in Fig. 18a and 18b, a single convective roll (corresponding to a mode with (aa) symmetry) is visible. This roll, pervasive through the entire extension of the cavity and representing the dominant circulation system, may be regarded as a classical manifestation of the so-called 'large-scale circulation' (LSC) typical of turbulent RB convection ([26] and all references therein). This large scale flow is generally produced by the merging of vortices with smaller scale continuously produced in the fluid due to the 'eruptive' nature of the thermal boundary layers located on the cold and hot walls in contact with the liquid. These thermal boundary layers typically produce 'waves' which travel in a direction parallel to the thermally-active (hot or cold) wall. These traveling disturbances cause local perturbations in the thickness of the boundary layer, which grow with time and are gradually transformed into thermal plumes. Thermal plumes tend to detach from the boundary layers and transport the vorticity associated with their cap (typically in the form of a toroidal vortex) to the center of the cavity, where all these vortices finally coalesce producing the almost 2D convection visible in Fig. 18a. The LSC, in turn, supports the development of waves in the boundary layers, which travel in the same direction of fluid transported by the LSC.

As witnessed by Fig. 17a, however, this mechanism can be deeply altered by strong heat exchange occurring through the lateral walls. The

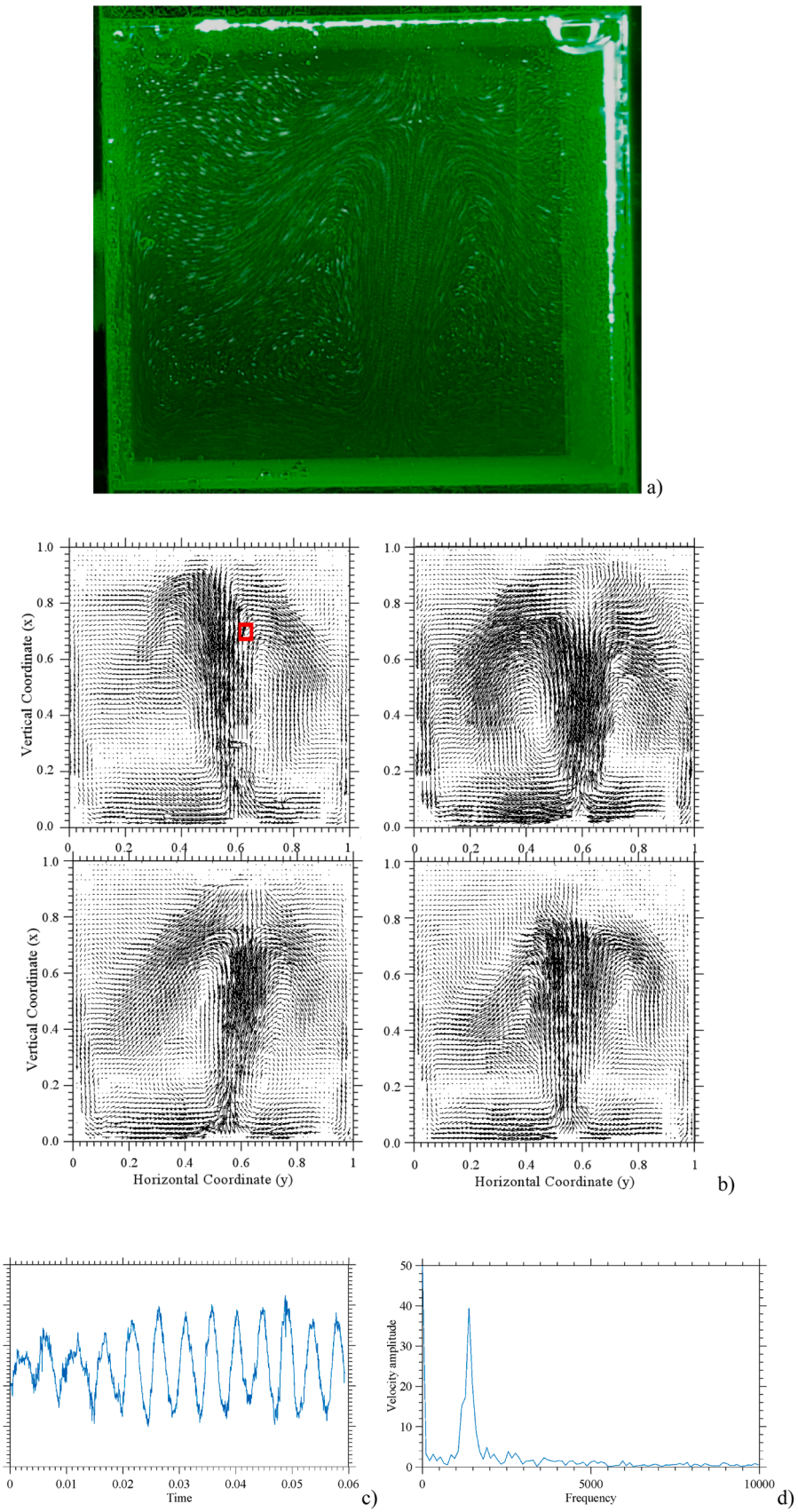

Fig. 17. Experimental picture (long-exposure with exposure time ≅ 0.7 s) (a), four snapshots of velocity field (b), related non-dimensional velocity signal (c) extracted using PIV and associated frequency spectrum (d) for $T_{cold} = 60$ °C, $\Delta T = 20$ K, Ra=8.7×10^7. The red square indicates the location from where the signal has been extracted.

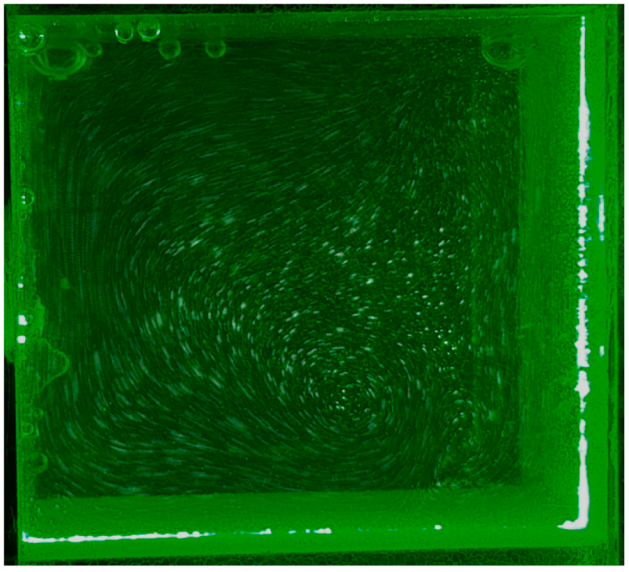

a)

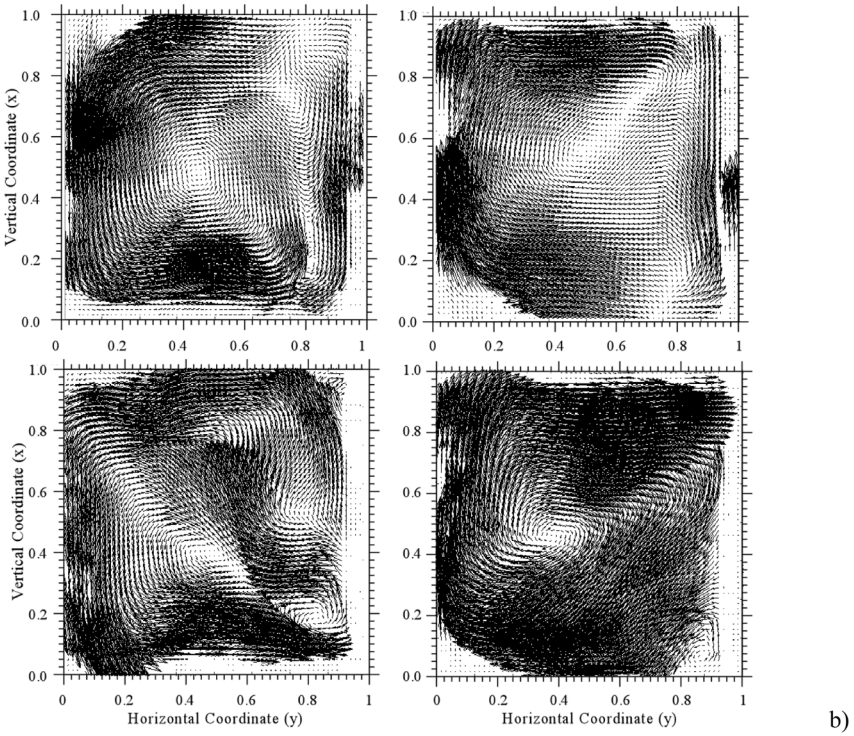

b)

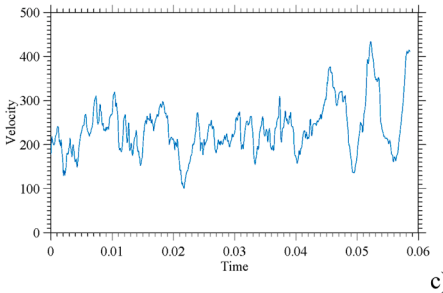

c)

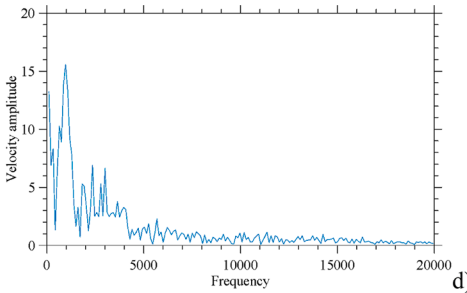

d)

Fig. 18. Experimental picture (long-exposure with exposure time ≅ 0.7 s) (a), four snapshots of velocity field (b) and related non-dimensional velocity signal (c) extracted using PIV (probe at $x = 3/4$ and $y = 1/2$) and associated frequency spectrum (d) for $T_{\text{cold}} = 20$ °C, $\Delta T = 20$ K, Ra=1.8×10^7.

cooled fluid descending along the lateral walls forces the pattern to develop a structure with a single thermal plume rising at the center. This effect also prevents the boundary layers from supporting the continuous propagation of waves thereby limiting the continuous (unsteady) production of small-scale plumes. Additional details about the unsteady behavior of the single central thermal plume in the case $T_{\mathrm{cold}} = 60\ ^{\circ}\mathrm{C}$ are provided in Sect. 4.3 on the basis of dedicated 3D numerical simulations and the evaluation of the related correlation dimension.

As a concluding remark for this section, we wish to highlight that, from a qualitative standpoint, the stabilization of 3D flow with respect to the equivalent 2D situation could have been anticipated on the basis of the existing previous literature for the adiabatic and conducting walls. As an example, in the numerical studies by [62] and [63] for a cubical box with adiabatic vertical walls, the critical Rayleigh number was found to be larger than that required by the corresponding two-dimensional case and this was ascribed to the presence of solid walls along the third dimension, which tend to introduce additional frictional effects, thereby stabilizing the flow with respect to 2D models. For the 3D cube with vertical conducting walls [64] found *an even larger value* of the Rayleigh number, which they interpreted as the tendency of systems with conducting sides to be more stable than the companion cases with adiabatic boundaries due to the ability of conducting walls to dissipate

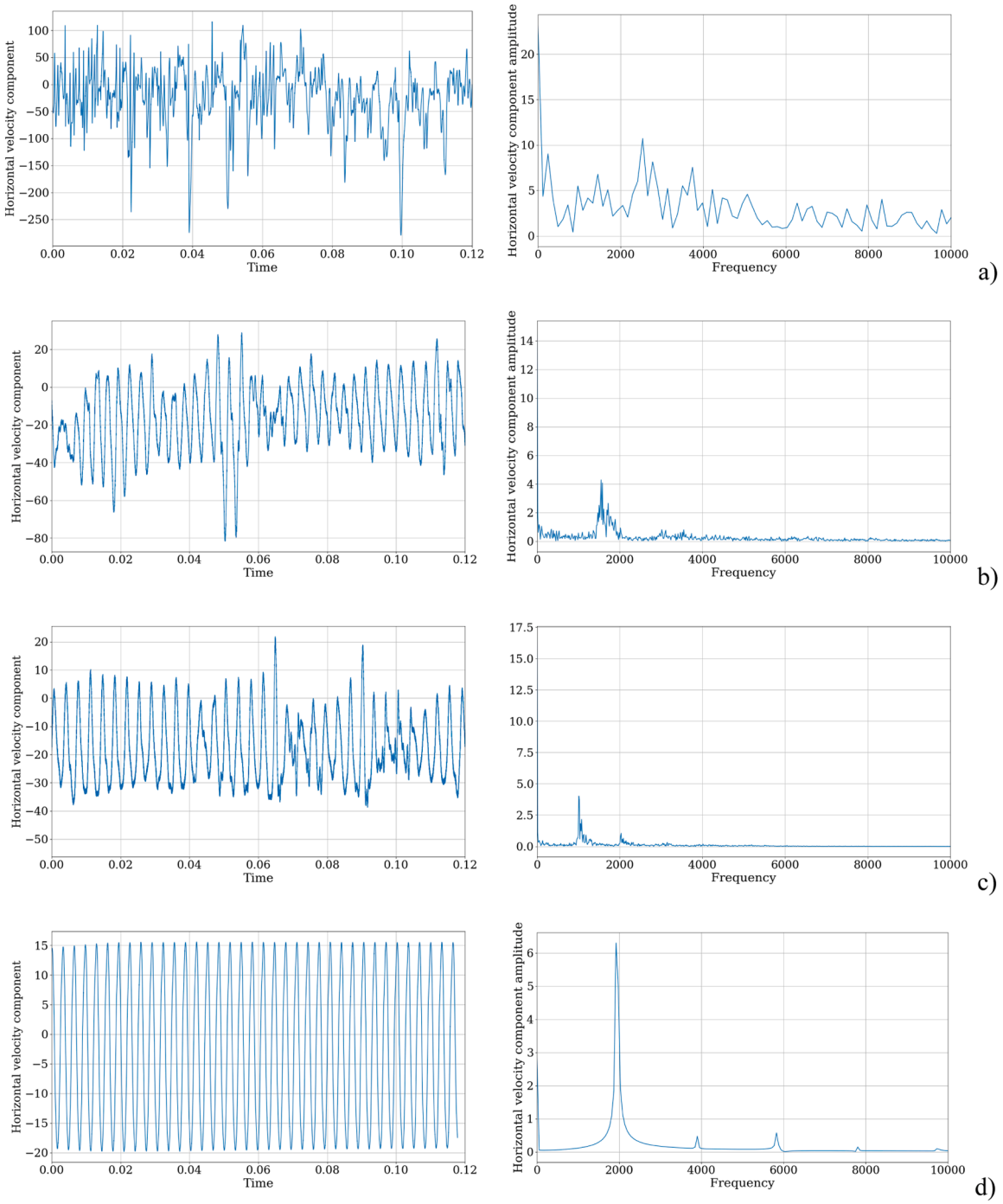

Fig. 19. 3D numerical results: Horizontal velocity component as a function of time (left) and related frequency spectrum (right) at $x = 1/2$, $y = 1/2$, $z = 5/8$ and T_{cold}=60 °C (Ra=8.74×10^{7}): a) Bi=2.1, b) Bi=4.2, c) Bi=6.3, d) Bi=10.56. Starting from a situation with chaotic behavior, the flow undergoes a gradual stabilization until a perfectly time-periodic state is recovered.

temperature perturbations.

4.3. Three-dimensional numerical simulations

This section is devoted to the presentation of 3D numerical results, which are finally used to get other meaningful details and insights into aspects, which would otherwise be out of reach.

The considered cases refer to $T_{cold} = 60$ °C and Bi=2.1, 4.2, 6.3 and 10.56, corresponding to dimensional values of the convective coefficient $h = 10, 20, 30, 50$ W/(m^{2}K), respectively. All these cases are summarized in Fig. 19, where the velocity is shown at a fixed point as a function of time. These figures are instrumental in demonstrating that, in line with the trends revealed by the experiments, an increase in the heat exchange rate produces a stabilization of the flow, which evolves from fully turbulent conditions for the lowest Biot number considered (2.1) to a regular oscillatory flow at Bi=10.56 (Fig. 19d).

This evolution is further witnessed by the related correlation dimension reported for the sake of completeness in Fig. 20. Interestingly, D spans the interval between 5.6 and 1, as the system evolves from the condition shown in Fig. 19a to that shown in Fig. 19d.

Additional useful information on these cases can be extracted from Table 9, where the difference between the nominal Rayleigh number and the effective one has been reported. Even though all cases have been simulated for a fixed Ra of 8.74×10^7 (ΔT =20 K), the variation of Ra_{eff} is very remarkable: passing from a positive value for Bi=2.1 to a negative one at Bi=10.56. An explanation for this effect can be elaborated in its simplest form using the same arguments already provided in Sect. 4.1 about the structure and location of the return flow and the cold fluid it carries as a result of the interaction with the vertical walls.

At this stage, it is also worth developing further the discussion about the *symmetries* of the flow already undertaken in that section under the constraint of two-dimensionality. When the third dimension is considered, the problem becomes obviously more complex because a variety of symmetries are possible and yet multiple solutions can be produced depending on the considered initial conditions.

Relevant information about the distinct influence of adiabatic or conducting walls on the multiplicity of solutions and the typical evolutionary path followed by these systems can yet be found in the literature. Interestingly, the excellent analysis by [65] identified several distinct branches of possible supercritical stationary states for various values of the Prandtl number (Pr = 0.71, 10, 130, see also [9] for Pr=0.01). These modes were found to display different preferred directions and to emerge in the form of straight rolls aligned with one of the vertical walls

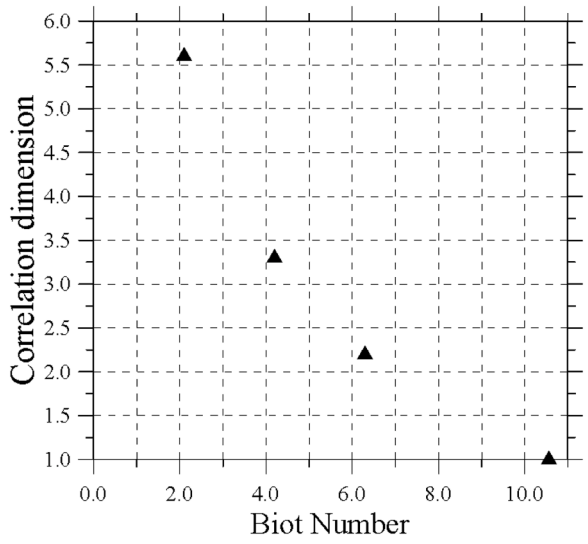

Fig. 20. Correlation dimension as a function of the Biot number for $T_{cold} = 60$ °C and $Ra=8.74\times10^7$ (3D cases).

Table 9
Effective Rayleigh numbers as a function of Bi for $T_{cold} = 60$ °C and $Ra=8.74\times10^7$.

Bi	Ra_{eff}
2.1	1.855×10^6
4.2	-2.02×10^6
6.3	-4.682×10^6
10.56	-7.794×10^6

or oriented along one of the diagonals or to take the configuration of a *toroidal vortex*. Moreover, according to these studies, when convection in the cubical geometry with adiabatic walls becomes oscillatory for $Ra>10^5$ and $Ra>1.2\times10^5$ for the Pr=0.01 and Pr=0.71 cases, respectively, the final state of the system is typically represented by an oscillating pattern with a single roll oriented along the direction of one of the sidewalls (i.e. along x or along y). [66] obtained similar results for Pr=130 and Rayleigh number up to 1.5×10^5. Interestingly, these authors found that six flow patterns are possible and that two, three, or even four of these patterns can coexist over certain ranges of Ra in the studied domain (multiple solutions).

Given these premises, in line with the similar arguments elaborated in Sect. 4.1, the present results do confirm that the heat transfer through the sidewalls can have a huge impact on the nature and symmetry of the convective modes selected by the system. This argument is substantiated in Fig. 21. This figure is useful as it shows that, like the 2D case, only one of the possible flow symmetries survives, namely that with the toroidal vortex, which corresponds to a single rising plume originating from the bottom hot wall.

The unsteady behavior of the central plume can also be directly inferred from this figure. It can be seen that the central jet (plotted in terms of isosurfaces of the vertical velocity component) undergoes a well-defined sequence of stages of evolution in time. While in panel (a), the central (rising) current of fluid displays a well-defined morphology, which aligns essentially with the $y = z$ diagonal direction, in panel (b) this direction has apparently undergone a 90° rotation. Taken together, these snapshots indicate that the time-periodic behavior of the flow in this case essentially stems from a kind of pulsating mechanism of the central rising current, which expands and shrinks periodically along the $y = z$ direction and the other diagonal direction.

For the purpose of quantifying the impact on the flow symmetry of the heat exchange through the lateral walls with respect to ideal adiabatic conditions, in Fig. 22 the case with Bi=10.56 is directly compared with equivalent numerical simulations conducted assuming the *classical adiabatic conditions* (Bi=0). In this figure the strong difference between these two situations can also be clearly seen in terms of features of the temperature field. In particular, the key to interpreting these results lies in considering that while in the adiabatic case, the morphology of the thermal plumes is extremely involved (Fig. 22a), with several rising and descending interacting plumes distributed throughout the cavity, for Bi=10.56, their structure is much more regular with rising hot plumes being concentrated in the center of the cavity (Fig. 22b).

Side-by-side 3D simulations and experiments are finally shown for the same case (Bi = 10.56 and T_{cold}=60 °C) in Fig. 23, where the streamlines have been drawn in the x-y plane: in both cases the tendency of the flow to create a well-defined central rising thermal plume is evident.

Table 10 is finally devoted to a comparison of the non-dimensional main frequencies (corresponding to the main peak of the spectrum) for experiments and numerical simulations from which we conclude that experiments and numerically determined frequencies are in good agreement when Bi ≅ 4 [whereas smaller values of Bi, e.g., Bi=2.1 (not shown) tend to produce irregular flow].

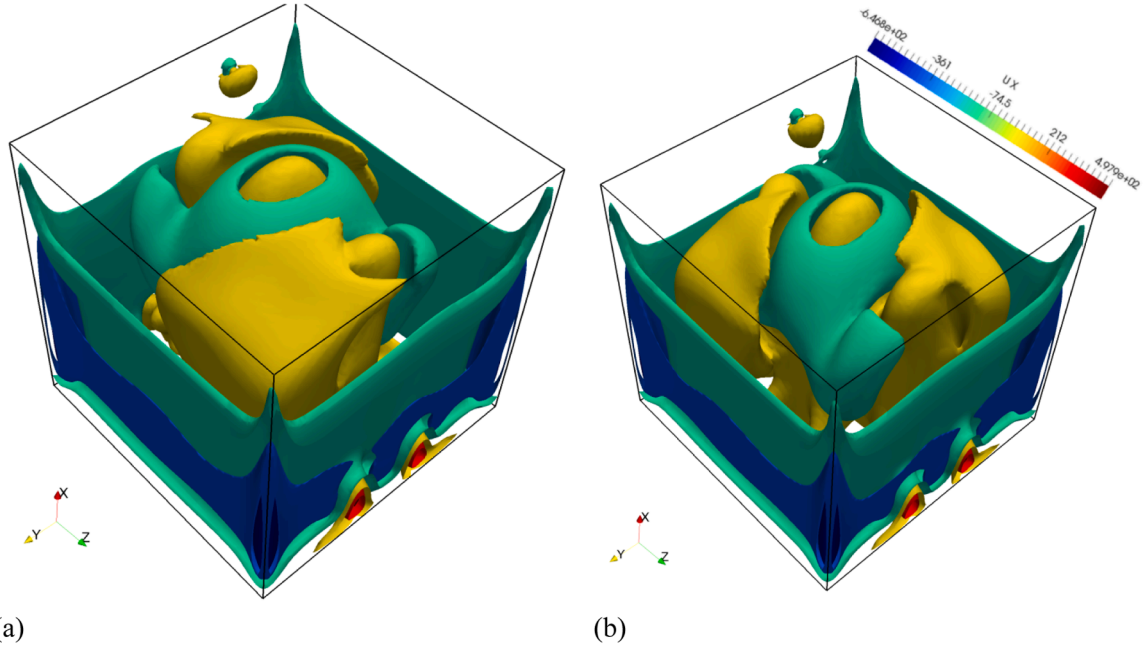

Fig. 21. Two snapshots of vertical velocity evenly distributed along the oscillation period at Ra=8.74×10^7, Bi=10.56 and T_{cold} = 60 °C (grid 100×100×100).

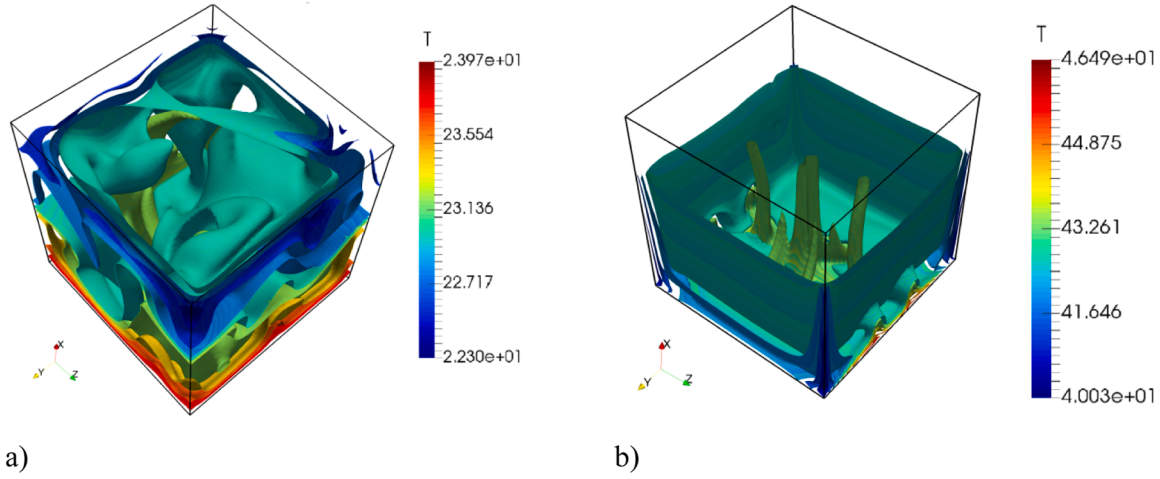

Fig. 22. Temperature isosurfaces: a) Cavity with adiabatic walls at Ra=178x10^6. b) 3D simulation at Bi=10.56 and T_{cold}=60 °C, Ra=8.74×10^7, Ra_{eff}=−7.794×10^6 (grid 100×100×100).

5. Conclusions

Thermal convection is a very complex non-linear problem where both initial and boundary conditions can have a remarkable impact on the emerging solutions and the related 'multiplicity'. In particular, of special interest in finite-size systems is the thermal behavior of the sidewalls because, by allowing thermal energy to leave or remain in the fluid domain, these can promote or prevent the evolution of the system along certain paths. The overarching aim of the present study was, therefore, to open up for such inquiry, by exposing and exploring critical issues as they emerge when one tries to deal with an experimental investigation of these problems.

Trying to summarize the main outcomes of the present study is not an easy task given its involved nature and the complexity of the obtained results. Anyhow, focusing on the most salient aspects, the following conclusions may be reported.

As a fruitful alternative to standard models with adiabatic or conducting walls, traditionally used to obtain insights into the effect of the heat exchange taking place through the lateral wall, a minimal model has been considered consisting of a fixed quantity of fluid encapsulated into a shell delimited by mutually perpendicular walls (cubic shape) with non-negligible thickness. The external vertical walls of this shell have been assumed to exchange heat with the external environment with the two external horizontal surfaces maintained at different constant temperatures.

According to the numerical results, starting from the idealized situation in which the flow is simulated in the framework of 2D computations, a variation in the intensity of the heat flux at the sidewalls can cause a significant departure from the equivalent dynamics that are produced when the idealized adiabatic or conducting boundary conditions are considered. Multiple solutions can still be an intrinsic feature of flow in these systems and the interaction among these multiple states can produce interesting phenomena such as attractor crisis, sudden transition to chaos and switching from the classical Ruelle-Takens scenario to the Curry-Yorke one. Nevertheless, heat exchange with the external environment can force these systems to select convective modes

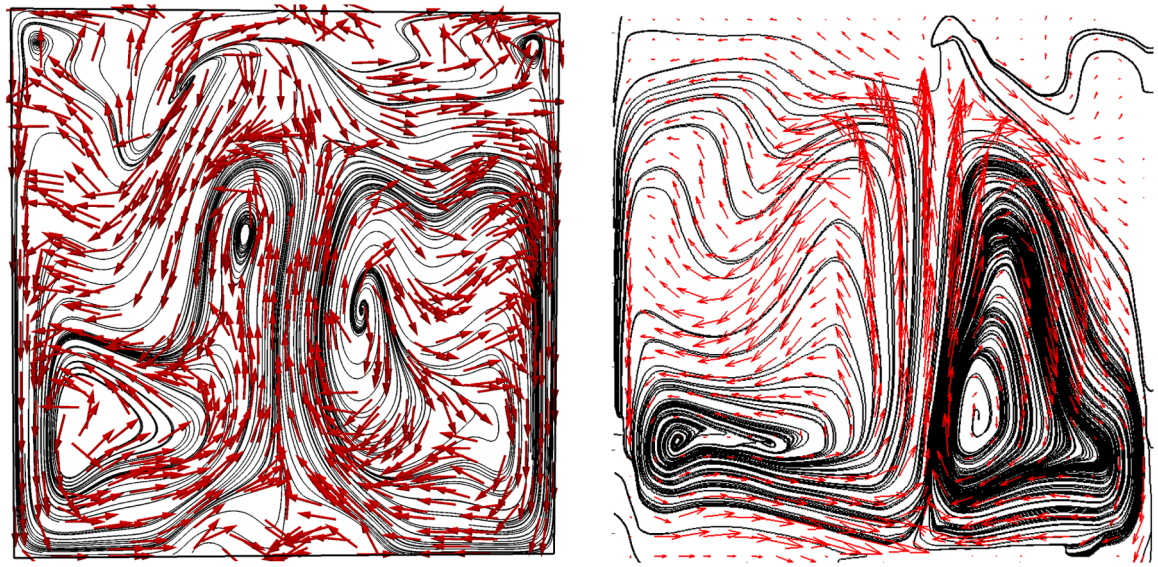

Fig. 23. Streamlines for T_{cold}=60 °C in the x-y plane (z=5/8) : a) 3D simulation for Bi=10.56; b) Experiment.

Table 10
Non-dimensional frequency and dimensional period in seconds as function of the Biot number. T_{cold} = 60 °C , Ra=8.74×10^7.

Bi	Non-dimensional angular freq.	Dimensional period [s]
Experiments	1488	42.7
4.2	1701	37.4
6.3	1763	36.0
10.56	1926	33

with a specific symmetry.

Dedicated experiments and dedicated three-dimensional simulations have confirmed that the striking shrinkage in the possible flow symmetries of the convective modes reported under the constraint of 2D flow is still a feature when the effects of the third dimension are taken into account. Moreover, in these cases, the increased amount of heat lost through the additional two walls limiting the fluid along the third direction can be responsible for significant stabilization with respect to the equivalent 2D cases.

When turbulent states are considered, which display a large scale circulation with prevailing two-dimensional structure ((aa) symmetry), on increasing the heat loss through the lateral walls, these tend to be replaced by much more regular modes of convection, corresponding to a roll with toroidal morphology, which gradually evolves from a time-periodic state to high-dimensional chaos in the limit as the Biot number tends to zero. Table 6 Eqs. (6), (9), (10a)-(10b), (11), (13)

CRediT authorship contribution statement

Hermes Ferialdi: Visualization, Validation, Software, Methodology, Data curation. **Marcello Lappa:** Writing – review & editing, Writing – original draft, Supervision, Project administration, Investigation, Formal analysis, Conceptualization.

Declaration of competing interest

The authors declare that they have no known competing financial interests or personal relationships that could have appeared to influence the work reported in this paper.

Data availability

Data will be made available on request.

Supplementary materials

Supplementary material associated with this article can be found, in the online version, at doi:10.1016/j.physd.2024.134190.

References

[1] T. Lyubimova, K. Rushinskaya, N. Zubova, Onset and nonlinear regimes of convection of a binary mixture in rectangular cavity heated from below, Microgravity Sci. Technol. 32 (2020) 961–972, https://doi.org/10.1007/s12217-020-09823-x.
[2] D. Melnikov, A. Mialdun, V. Shevtsova, Peculiarity of 3D flow organization in Soret driven instability, J. Non-Equilibr. Thermodyn. 32 (3) (2007) 259–270.
[3] B. Seta, J. Gavalda, M.M. Bou-Ali, X. Ruiz, C. Santamaria, Determining diffusion, thermodiffusion and Soret coefficients by the thermogravitational technique in binary mixtures with optical digital interferometry analysis, Int. J. Heat Mass. Transf. 147 (2020) 118935.
[4] B. Seta, A. Errarte, I.I. Ryzhkov, M.M. Bou-Ali, V. Shevtsova, Oscillatory instability caused by the interplay of Soret effect and cross-diffusion, Phys. Fluids 35 (2) (2023) 021702.
[5] P. Bontoux, B. Roux, G.H. Schiroky, B.L. Markham, F. Rosenberger, Convection in the vertical midplane of a horizontal cylinder. Comparison of two-dimensional approximations with three-dimensional results, Int. J. Heat Mass Transf. 29 (2) (1986) 227–240.
[6] A.Yu. Gelfgat, Different modes of Rayleigh–Bénard instability in Two- and three-dimensional rectangular enclosures, J. Comput. Phys. 156 (1999) 300–324.
[7] M. El Ganaoui, A. Lamazouade, P. Bontoux, D. Morvan, Computational solution for fluid flow under solid/liquid phase change conditions, Comput. Fluids 31 (4–7) (2002) 539–556.
[8] R. Bennacer, M. El Ganaoui, E. Leonardi, Symmetry breaking of melt flow typically encountered in a Bridgman configuration heated from below, Appl. Math Model 30 (11) (2006) 1249–1261.
[9] M. Lappa, On the nature and structure of possible three-dimensional steady flows in closed and open parallelepipedic and cubical containers under different heating conditions and driving forces, Fluid Dyn. Mater Process 1 (1) (2005) 1–19, https://doi.org/10.3970/fdmp.2005.001.001.
[10] M. Lappa, Secondary and oscillatory gravitational instabilities in canonical three-dimensional models of crystal growth from the melt, Part1: rayleigh-Bènard systems, Comptes Rendus Mécanique 335 (5–6) (2007) 253–260, https://doi.org/10.1016/j.crme.2007.05.003.
[11] M.R. Benoit, R.B. Brown, P. Todd, E.S. Nelson, D.M. Klaus, Buoyant plumes from solute gradients generated by non-motile Escherichia coli, Phys. Biol. 5 (4) (2008) 046007.

[12] R. Delgado-Buscalioni, E. Crespo del Arco, Stability of thermally driven shear flows in long inclined cavities with end-to-end temperature gradient, Int. J. Heat Mass Transf.. 42 (1999) 2811–2822.
[13] T. Yanagisawa, Y. Yamagishi, Rayleigh–Bénard convection in spherical shell with infinite Prandtl number at high Rayleigh number, J. Earth Simulator 4 (2005) 11–17.
[14] G.A. Glatzmaier, P.H. Roberts, Simulating the geodynamo, Contemp. Phys. 38 (1997) 269–288.
[15] R. Rotunno, The fluid dynamics of tornadoes, Annu Rev Fluid Mech. 45 (2013) 59–84.
[16] K. Heng, A.P. Showman, Atmospheric dynamics of hot exoplanets, Annu. Rev. Earth Planet Sci. 43 (2015) 509–540.
[17] Rayleigh Lord, On the convection currents in a horizontal layer of fluid when the higher temperature is on the underside, Phil. Mag. 32 (1916) 529–546.
[18] A. Schlüter, D. Lortz, F.H. Busse, On the stability of steady finite amplitude convection, J. Fluid Mech. 23 (1965) 129–144.
[19] R.M. Clever, F.H. Busse, Transition to time-dependent convection, J. Fluid Mech. 65 (1974) 625–645.
[20] F.H. Busse, Nonlinear properties of thermal convection, Rep. Prog. Phys. 41 (1978) 1929–1967.
[21] F.H. Busse, R.M. Clever, Instabilities of convection rolls in a fuid of moderate Prandtl number, J. Fluid Mech. 91 (1979) 319–335.
[22] J.M. Luijkx, J.K. Platten, On the onset of free convection in a rectangular channel, J. Non-EquilibriumThermodynam. 6 (1981) 141–158.
[23] I. Goldhirsch, R.B. Pelz, S.A. Orszag, Numerical simulation of thermal convection in a two-dimensional finite box, J. Fluid Mech. 199 (1989) 1–28.
[24] J. Mizushima, Onset of thermal convection in a finite twodimensional box, J. Phys. Soc. Jpn. 64 (1995) 2420–2432.
[25] F. Stella, E. Bucchignani, Rayleigh–Bénard convection in limited domains: part 1 – oscillatory flow, *Numer. Heat Transf.*, Part A 36 (1) (1999) 1–16.
[26] M. Lappa, Some considerations about the symmetry and evolution of chaotic Rayleigh–Bénard convection: the flywheel mechanism and the “wind” of turbulence, Comptes Rendus Mécanique 339 (2011) 563–572, https://doi.org/10.1016/j.crme.2011.05.002.
[27] M. Lappa, A Mathematical and Numerical Framework for the Analysis of Compressible Thermal Convection in Gases at very high Temperatures, J Comput Phys 313 (2016) 687–712, https://doi.org/10.1016/j.jcp.2016.02.062.
[28] M. Lappa, Thermal Convection: Patterns, Evolution and Stability, John Wiley & Sons, Ltd, Chichester, England, 2009.
[29] M. Lappa, Rotating Thermal Flows in Natural and Industrial Processes, John Wiley & Sons, Ltd, Chichester, England, 2012.
[30] M. Lappa, On the existence and multiplicity of one-dimensional solid particle attractors in time-dependent rayleigh-bénard convection, Chaos 23 (1) (2013) 013105, https://doi.org/10.1063/1.4773001.
[31] M. Lappa, On the transport, segregation and dispersion of heavy and light particles interacting with rising thermal plumes, Phys. Fluids 30 (3) (2018) 033302.
[32] D. Gray, A. Giorgini, The validity of the Boussinesq approximation for liquids and gases, Int. J. Heat Mass Transf. 19 (5) (1976) 545–551.
[33] W. Rohsenow, J. Hartnet, Y. Cho, Handbook of Heat Transfer (3rd Edition), McGraw-Hill, 1998.
[34] Incropera, Fundamentals of Heat and Mass Transfer, 6th Edition, Wiley, 2007.
[35] R.I. Issa, Solution of the implicitly discretized fluid flow equations by operator-splitting, J. Comp. Phys. 62 (1986) 40–65.
[36] F. Moukalled, L. Mangani, M. Darwish, The Finite Volume Method in Computational Fluid Dynamics: An Advanced Introduction with OpenFOAM and Matlab, Springer International Publishing, 2016.
[37] C.M. Rhie, W.L. Chow, Numerical study of the turbulent flow past an airfoil with trailing edge separation, AIAA J 21 (1983) 1525–1532.
[38] K. Ferialdi, M. Lappa, C. Haughey, On the role of thermal boundary conditions in typical problems of buoyancy convection: a combined experimental-numerical analysis, Submitted (2020).
[39] N. Ouertatani, N.B. Cheikh, B.B. Beya, T. Lili, Numerical simulation of two-dimensional Rayleigh-Benard convection in an enclosure, C.R. Mecanique 336 (5) (2008) 464–470.
[40] C.Y. Soong, P.Y. Tzeng, D.C. Chiang, T.S. Sheu, Numerical study on mode-transition of natural convection in differentially heated inclined enclosures, Int. J. Heat Mass Transf. (1995). http://link.aip.org/link/?CHA/23/013105.
[41] U. Kurzweg, Convective instability of a hydromamagnetic fluid within a rectangular cavity, Int. J. Heat Mass Transf. 8 (1965) 35–41.
[42] W. Velte, Stabilitatsverhalten und Verzweigung stationarer Losungen der Navier-Stokesschen Gleichungen, Arch. Rat. Mech. Anal. 16 (2) (1964) 97–125.
[43] M.S. Chana, P.G. Daniels, Onset of Rayleigh–Bénard convection in a rigid channel, J. Fluid Mech. 199 (1989) 257–279.
[44] J. Mizushima, T. Adachi, Sequential transitions of the thermal convection in a square cavity, J. Phys. Soc. Jpn. 66 (1) (1997) 79–90.
[45] S. Newhouse, D. Ruelle, T. Takens, Occurrence of strange axiom-a attractors near quasi-periodic flows on T^m, m≥3, Commun. Math. Phys. 64 (1978) 35–40.
[46] J. Balatoni, A. Renyi, Publ. Math. Inst. Hung. Acad. Sci, 1, 9, in: Hungarian) [translation: Selected papers of A. Renyi, 1, Budapest Academy, 1956, p. 558, 1976].
[47] J. Theiler, Spurious dimension from correlation algorithms applied to limited time-series data, Phys. Rev. A 34 (3) (1986) 2427–2432.
[48] P. Grassberger, Generalized dimensions of strange attractors, Phys. Lett. A 97 (6,5) (1983) 227–230.
[49] P. Grassberger, I. Procaccia, Characterization of strange attractors, Phys. Rev. Lett. 50 (1983) 346–349.
[50] P. Grassberger, I. Procaccia, Measuring the strangeness of strange attractors, Phys. D 9 (1983) 189–208.
[51] J.P. Gollub, S.V. Benson, Many routes to turbulent convection, J. Fluid Mech. 100 (1980) 449–470.
[52] A. Libchaber, C. Laroche, S. Fauve, Period doubling cascade in mercury, a quantitative measurement, J. Physique Lett. 43 (1982) 211–216.
[53] F. Stella, E. Bucchignani, Rayleigh–Bénard convection in limited domains: part 2 – transition to chaos", *Numer. Heat Transf.*, Part A 36 (1) (1999) 17–34.
[54] H. Curry, J.R. Herring, J. Loncaric, S.A. Orszag, Order and disorder in two- and three-dimensional Bénard convection, J. Fluid Mech. 147 (1984) 1–38.
[55] M. Lappa, H. Ferialdi, Multiple solutions, Oscillons and strange attractors in thermoviscoelastic marangoni convection, Phys. Fluids 30 (10) (2018) 104104.
[56] S. Paul, M.K. Verma, P. Wahi, S.K. Reddy, K. Kumar, Bifurcation analysis of the flow patterns in two-dimensional Rayleigh–Bénard convection, Int. J. of Bifurcation and Chaos 22 (5) (2012).
[57] C. Grebogi, E. Ott, A.J. Yorke, Crises, sudden changes in chaotic attractors, and transient chaos, Phys. D: Nonlinear Phenomena 7 (1–3) (1983) 181–200.
[58] M. Kitano, T. Yabuzaki, T. Ogawa, Symmetry-recovering crises of chaos in polarization-related optical bistability, *Phys. Rew.* A 29 (3) (1984).
[59] J. Curry, J.A. Yorke, A transition from Hopf bifurcation to chaos: computer experiments with maps R2, in The structure of attractors in dynamical systems, Springer Notes Math. 668 (1977) 48.
[60] M. Lappa, H. Ferialdi, Gravitational thermal flows of liquid metals in 3d variable cross-section containers: transition from low-dimensional to high-dimensional chaos, Chaos 28 (2018) 093114.
[61] F. Camastra, A. Vinciarelli, Intrinsic Dimension estimation of data: an approach based on grassberger–procaccia’s algorithm, Neural Process. Lett. 14 (2001) 27–34, https://doi.org/10.1023/A:1011326007550.
[62] J. Mizushima, T. Nakamura, Onset of Three-dimensional thermal convection in a rectangular parallelepiped cavity, J. Phys. Soc. Jpn. 72 (2) (2003) 197–200.
[63] D. Puigjaner, J. Herrero, F. Giralt, C. Simó, Stability analysis of the flow in a cubical cavity heated from below, Phys Fluids 16 (10) (2004) 3639–3655.
[64] J. Mizushima, O. Matsuda, Onset of 3D thermal convection in a cubic cavity, J. Phys. Soc. Jpn. 66 (8) (1997) 2337–2341.
[65] J. Pallares, F.X. Grau, F. Giralt, Flow transitions in laminar Rayleigh–Bénard convection in a cubical cavity at moderate Rayleigh numbers", Int. J. Heat Mass Transfer 43 (1999) 753–769.
[66] D. Puigjaner, J. Herrero, F. Giralt, C. Simó, Bifurcation analysis of multiple steady flow patterns for Rayleigh–Bénard convection in a cubical cavity at Pr=130, Phys. Rev. E 73 (2006) 046304.